Nanoscale

ROYAL SOCIETY OF CHEMISTRY

PAPER

View Article Online
View Journal | View Issue

Check for updates

Cite this: *Nanoscale*, 2025, **17**, 16457

Electrochemical analysis of flexible symmetric supercapacitors using WSe_2@graphite thin film electrodes under different pH conditions†

Akshay Tomar, [a] Nitesh Choudhary, [a] Radhika Jain, [a] Dushyant Chaudhary, [a] Gaurav Malik, [b] Sheetal Issar [a] and Ramesh Chandra *[a]

A key focus of this research is to investigate the influence of electrolyte pH on the supercapacitive performance of a flexible symmetric supercapacitor (SS) based on WSe_2@graphite composite electrodes. To represent distinct pH environments, three aqueous electrolytes, namely H_2SO_4 (acidic), NaOH (basic), and Na_2SO_4 (neutral), were selected. A range of standard characterization methods, including X-ray diffraction (XRD), field emission scanning electron microscopy (FE-SEM), X-ray photoelectron spectroscopy (XPS), atomic force microscopy (AFM), and energy-dispersive X-ray spectroscopy (EDX), were employed to validate the successful fabrication and integrity of the supercapacitive electrode. Electrochemical performance was evaluated through cyclic voltammetry (CV), galvanostatic charge–discharge (GCD) and electrochemical impedance spectroscopy (EIS), elucidating the charge storage behaviour of the device at different pH levels. As a result, the fabricated SS device exhibited an impressive electrochemical potential window of 2 V (0 to +2 V) across all electrolytic systems, demonstrating excellent operational stability and pH adaptability. Among the tested electrolytes, the acidic H_2SO_4 electrolyte demonstrated the highest performance, achieving a high areal capacitance of 123.73 mF cm^{-2} and an energy density of 68.73 μWh cm^{-2} at a current density of 1 mA cm^{-2}. Furthermore, the device demonstrated reliable cycling stability, retaining approximately 78.69% of its initial capacitance after 5000 consecutive GCD cycles. These results highlight the critical role of electrolyte pH in tailoring supercapacitor performance and provide valuable insights into the design of high-performance, flexible symmetric supercapacitors through strategic electrolyte selection.

Received 1st April 2025,
Accepted 11th June 2025

DOI: 10.1039/d5nr01328c

rsc.li/nanoscale

Published on 24 2568. Downloaded on 7/6/2569 10:33:39.

1 Introduction

The demand for advanced energy storage systems has increased significantly in recent years, driven by the rapid advancement of renewable energy technologies, electric vehicles, and portable electronics.[1,2] Among the diverse range of energy storage systems, supercapacitors have garnered significant interest from researchers because of their ability to merge the best advantageous characteristics of both batteries and conventional capacitors, resulting in high power density, rapid charge–discharge rates, and long cycle life.[3–5] However, the selection of a suitable electrode material has a substantial impact on the effectiveness of supercapacitors.[6–9] Transition metal dichalcogenides (TMDCs) have emerged as promising electrode materials due to their unique layered structure, tunable electrical properties, superior electrochemical stability, and cost-effectiveness.[10–13] Among the various TMDCs, tungsten diselenide (WSe_2) has demonstrated encouraging performance in energy storage applications.[14–16] WSe_2 is a semiconducting material with a two-dimensional layered structure stacked together by weak van der Waals interactions, like graphene, and can be easily exfoliated mechanically into thin sheets. These ultra-thin films are perfect for use as electrode materials in high-performance supercapacitors, as their enormous surface area contributes to a very high theoretical capacitance and improved electrochemical performance.[17,18] However, their relatively low electrical conductivity and limited cycling stability pose challenges that hinder their practical implementation in supercapacitors.[19] To overcome these limitations, researchers have explored composite materials that integrate WSe_2 with highly conductive substrates. Among

[a]*Thin Film Lab, Institute Instrumentation Centre, Indian Institute of Technology Roorkee, Roorkee-247667, India. E-mail: ramesh.chandra@ic.iitr.ac.in*
[b]*Semiconductor Physics Research Centre, Jeonbuk National University, Jeonju, 561-756, Republic of Korea*

† Electronic supplementary information (ESI) available. See DOI: https://doi.org/10.1039/d5nr01328c

Published on 24 2568. Downloaded on 7/6/2569 10:33:39.

them, one of the promising composites is WSe_2@graphite, which consists of a WSe_2 thin film deposited over the graphite substrate. Graphite, renowned for its excellent electrical and thermal conductivity, mechanical robustness, and chemical stability, provides a conductive framework that enhances charge transport and mechanical stability. The composites formed by the thin layer of WSe_2 over graphite benefit from the synergistic properties of both materials. This combination not only enhances the overall conductivity of the electrode but also increases the electroactive surface area, thereby facilitating more efficient charge storage and accelerating ion transport. This result leads to increased capacitance and cycling stability compared to the individual components, making it a promising candidate for use in high-performance supercapacitors. Furthermore, the flexibility of graphite sheets plays a crucial role in the mechanical stability of the composite, thereby enhancing its performance under mechanical stress. This characteristic makes it ideal for application in contemporary flexible and wearable energy storage devices, which are becoming increasingly important in portable electronics and smart technologies.[20,21] The integration of the characteristics of these two composite materials, including the high surface area, adjustable band gap, and the relative abundance of WSe_2, combined with the flexibility, mechanical strength, and outstanding in-plane electrical conductivity of the graphite substrate, enables the development of electrodes that are both efficient and versatile for different form factors and operating conditions.[22,23]

Building on prior studies, this work presents a significant advancement in WSe_2@graphite supercapacitor electrodes through the optimization of the sputtering process to engineer a highly porous nano-cauliflower morphology.[24,25] This tailored nanostructure offers several advantages, including a substantially increased electrochemically active surface area for enhanced charge storage, optimized ion diffusion pathways for improved electrolyte accessibility, and superior charge transfer kinetics. As a result, the areal capacitance of the fabricated devices exhibits a nearly sevenfold (7×) enhancement compared to previously reported WSe_2@graphite thin films at the same scan rate.[24] These findings underscore the critical role of morphology engineering in dictating electrochemical performance and provide valuable insights into the rational design of advanced electrode architectures for high-efficiency supercapacitors.

While extensive research has been conducted on optimizing electrode materials, comparatively less emphasis has been placed on understanding the role of electrolytes in determining supercapacitor performance. The importance of electrolytes has been largely ignored, even though significant advancements have been made in enhancing energy density with novel electrode materials.[26] Electrolytes enable ion movement at the electrode–electrolyte interface, which directly influences the overall performance of the device, highlighting their vital role in supercapacitors. In the realm of electrochemical supercapacitor electrolytes, a diverse array of options has been investigated, including aqueous, organic, ionic liquids, redox-type, and solid or semi-solid electrolytes, leading to significant advancements over the past several decades.[27–29] The selection of appropriate electrolytes is contingent upon the size and mobility of ions within the electrode material; these characteristics subsequently affect the specific capacitance and energy density of the supercapacitor. An ideal electrolyte for energy storage systems typically demonstrates a wide potential window, elevated ionic conductivity, and robust chemical and electrochemical stability. It should remain non-reactive with the system components, such as electrodes, current collectors, and packaging, while ensuring compatibility with the electrode materials. Additionally, an extensive operating temperature range, minimal volatility, and decreased flammability are crucial for ensuring safety and adaptability. Furthermore, the electrolyte must be sustainable and economically viable.[30–33] Meeting all these criteria in a single electrolyte presents significant challenges, prompting in-depth investigations to enhance their performance and improve their integration into energy storage systems. The selection of electrolytes impacts the operating voltage window, ionic conductivity, and electrochemical stability, all of which are essential for optimizing energy density. Recent investigations indicate that various electrolyte characteristics, alongside electrode materials, can greatly influence the energy storage capacity of supercapacitors. To fully realize the potential of supercapacitor technology, it is essential to develop a comprehensive understanding of the interactions between electrolytes and electrode materials, especially in diverse environments.

The novelty of this work lies in the comprehensive investigation of the electrochemical performance of WSe_2@graphite-based supercapacitors in the presence of different aqueous electrolytes, specifically H_2SO_4, NaOH, and Na_2SO_4. This study systematically explores the influence of electrolyte pH on the capacitive behavior of WSe_2@graphite thin film electrodes, providing new insights into the interaction between the electrode material and the electrochemical environment. A key aspect of novelty is the evaluation of how different electrolyte environments, ranging from acidic to basic to neutral, affect the ionic transport dynamics, electrochemical stability, and charge storage mechanisms of WSe_2@graphite electrodes. This study not only elucidates the fundamental electrochemical properties of this composite material but also demonstrates how electrolyte selection can significantly modulate its performance in terms of specific capacitance, energy density, and cycling stability. By examining the effects of varying pH conditions, this work provides a deeper understanding of the interfacial phenomena occurring at the electrode–electrolyte interface, which is critical for optimizing the electrochemical performance of supercapacitors. Furthermore, this research highlights the potential of WSe_2@graphite as an electrode material that can operate effectively across a range of electrolyte compositions, showcasing its adaptability for different energy storage applications. The findings contribute to the broader field of energy storage by offering valuable insights into the synergistic effects of material properties and electrolyte chemistry, paving the way for the rational design of

 This journal is © The Royal Society of Chemistry 2025

Published on 24 2568. Downloaded on 7/6/2569 10:33:39.

next-generation supercapacitors with enhanced performance. By emphasizing the often-overlooked role of electrolytes, this study provides a more holistic approach towards the development of high-performance supercapacitors, bridging the knowledge gap between electrode material innovation and electrolyte optimization.

2 Experimental section

2.1 Materials and chemicals used

For this study, we utilized a circular target composed of tungsten diselenide (WSe_2) with a diameter of 6 cm and a thickness of 5 mm, along with highly flexible graphite sheets with 0.2 mm thickness and an area of 1 cm^2 as the substrate. The target material was purchased from Testbourne Ltd, UK, while the substrate was procured from UC Enterprises, India. High-purity chemicals used for electrochemical analysis such as hydrogen sulfate (H_2SO_4), sodium sulfate (Na_2SO_4), and sodium hydroxide (NaOH) were obtained from HiMedia Laboratories Pvt. Ltd, India. Argon gas required for the sputtering process was supplied by Sigma Gases, India. The installation of the sputtering system was carried out by Excel Instruments, India.

2.2 Thin film fabrication

The deposition of WSe_2 thin films onto the graphite substrate was carried out using the DC sputtering technique (Fig. 1), as detailed in our recent publication.[22] The optimized parameters and conditions for the sputtering deposition are provided in Table S1,† which are essential for achieving the desired film characteristics and performance.

The deposition of the WSe_2 thin film as an electrode material onto a graphite substrate was successfully conducted using a controlled DC sputtering process. The plasma-based deposition was performed at a power setting of 75 W in a high-vacuum environment, maintaining a base pressure of 3×10^{-6} Torr for 25 minutes to achieve a desired film thickness suitable for electrochemical analysis. This process involves the introduction of argon gas at a rate of 20 sccm, maintaining the operating pressure of the vacuum chamber at 10 mTorr. The substrate was kept at a temperature of 200 °C and the substrate and target materials were placed at a distance of 5 cm apart to ensure the desired morphological growth of the fabricated thin films. The goal of optimizing these deposition parameters was to achieve an appropriate balance between film thickness and quality.

2.3 Characterization

The crystallographic properties *i.e.*, phase, crystal structure, lattice parameters, and crystallite size of the fabricated thin film were determined using an X-ray diffractometer (Bruker AXS, D8 Advance). To assess the chemical state and relative abundance of the different elements present within the deposited material, X-ray photoelectron spectroscopy (XPS) was employed, utilizing Physical Electronics PHI 5000 Versa Probe III equipment. The structural and compositional analyses of the WSe_2 thin film were further assessed using transmission electron microscopy (TEM), high-resolution transmission electron microscopy (HR-TEM), selected area electron diffraction (SAED), and energy dispersive X-ray (EDX) spectroscopy with elemental mapping using a Talos™ F200X Feg TEM instrument. The surface morphology, elemental composition, distribution of elements, and cross-sectional thickness of the sputtered thin film were determined with a field emission scanning electron microscope (FE SEM, Carl Zeiss, Zeiss Gemini) and an energy-dispersive X-ray (EDX) spectrometer, with an X-ray detector provided by AMETEK. Surface area and porosity measurements were conducted using a QUANTACHROME AUTOSORB iQ-x multipoint surface area measurement instrument. The wetting properties (hydrophilicity/hydrophobicity), surface energy, and surface roughness of the deposited thin film were determined using the sessile drop method with contact angle goniometry, employing a Kruss 100 easy drop contact angle analyzer. The root mean square roughness (RMS) was characterized using a Bruker Dimension Icon AFM.

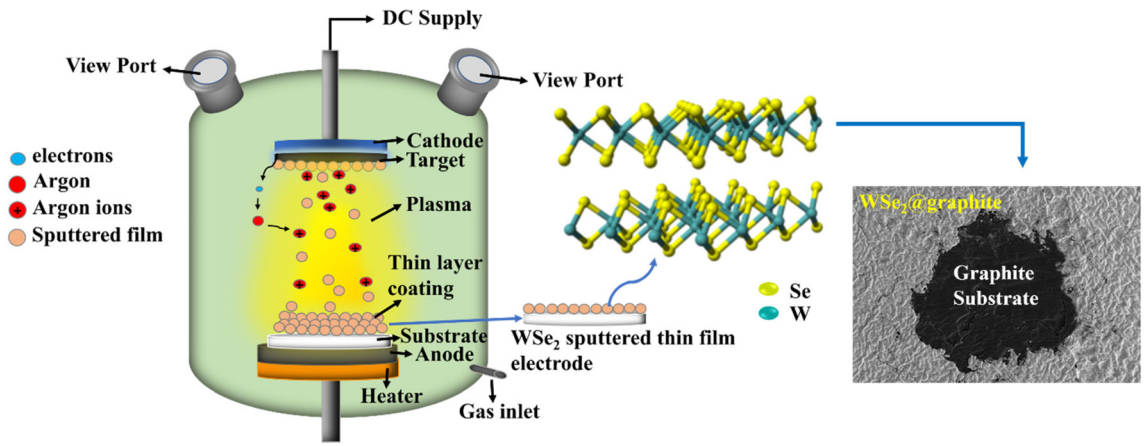

Fig. 1 Schematic representation of the sputtering chamber used for the deposition of the WSe_2 thin film over the graphite substrate.

Published on 24 2568. Downloaded on 7/6/2569 10:33:39.

Furthermore, the electrochemical performances including capacitance, energy density, and power density were determined using a Metrohm Autolab PGSTAT potentiostat/galvanostat electrochemical system.

3 Results and discussion

3.1 Structural and elemental analysis

The successful fabrication of a WSe_2 thin film on the graphite substrate was confirmed by X-ray diffraction (XRD) analysis. The red XRD pattern represents the WSe_2 thin films deposited over the graphite substrate, the black XRD pattern corresponds to the pure WSe_2 target material used for sputtering purposes, whereas the blue pattern corresponds to the pristine graphite substrate, as illustrated in Fig. 2(a). The diffraction peaks observed at 2θ values of 13.6°, 34.4°, and 37.8° indicated by a pink heart symbol correspond to the (002), (102), and (103) planes of the WSe_2 thin film, respectively. The presence of these peaks characterized by sharp and narrow full widths at half maximum (FWHMs) indicates that the WSe_2 films exhibit high crystallinity. These peaks are consistent with the 2H-type hexagonal phase of WSe_2, aligning with the space group *P*63/*mmc*, and match well with the JCPDS card no. 00-038-1388 as shown by the magenta pattern at the bottom of Fig. 2(a).

Additionally, the XRD pattern of WSe_2@graphite shows additional peaks attributable to the underlying graphite substrate, as evidenced by the blue XRD pattern. This distinction confirms that the observed peaks at the specified 2θ values are characteristic of the WSe_2 thin films, while the additional peaks are due to the presence of the graphite substrate.

Fig. 2(b–d) presents the XPS spectra of the WSe_2@graphite thin film electrode. XPS is a surface-sensitive analytical technique that helps to obtain information about the elemental composition, chemical state, and electronic environment of the materials.[34,35] XPS measurements were performed using a PHI 5000 VersaProbe III (Ulvac-Phi, Inc.) in ultrahigh vacuum conditions (2×10^{-7} Pa) with a monochromatic Al Kα source (energy = 1.48 keV), a step width of 0.05 eV, and a pass energy of 55 eV for elemental scans, while the survey spectrum was acquired with an energy of 280 eV. Both survey and high-resolution scans were carried out using raster scans, with a beam diameter of 100 μm and a neutralizer setting of 1.5 V and 20 μA. The base pressure was 8×10^{-8} Pa, and the non-conductive tape was used as the substrate material. For data analysis, MultiPak XPS software was used to perform peak fitting. The Shirley background subtraction method was

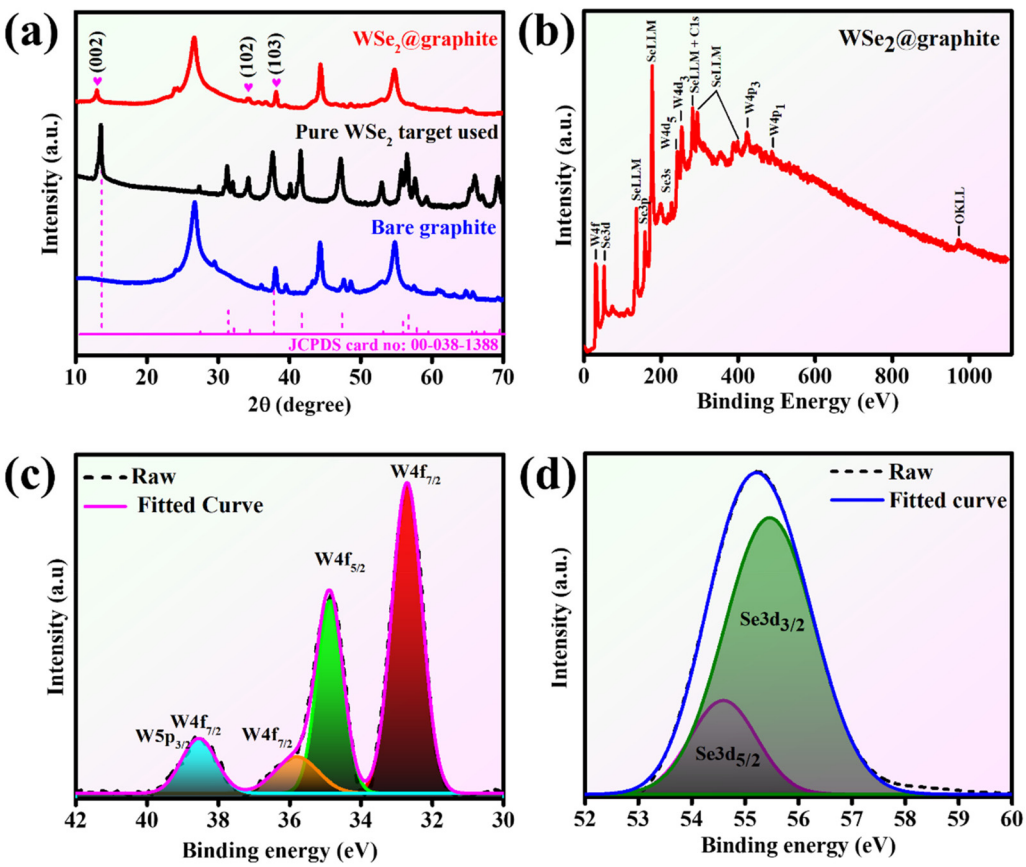

Fig. 2 (a) XRD patterns of pristine graphite sheets, pure WSe_2, and WSe_2@graphite thin films, (b) low resolution survey XPS spectra of the WSe_2@graphite thin film electrode, and high resolution XPS spectra of individual elements: (c) W4f and (d) Se3d.

This journal is © The Royal Society of Chemistry 2025

Published on 24 2568. Downloaded on 7/6/2569 10:33:39.

applied to remove the broad baseline arising from the inelastic scattering of photoelectrons. The peaks were assigned based on the expected binding energies of the elements under investigation. To facilitate accurate peak assignment, XPS spectra of pure graphite and pure WSe_2 (used as the target material) were acquired as reference spectra. These reference spectra, presented in Fig. S1,† provide a basis for identifying the elemental composition and chemical states within the WSe_2@graphite composite, thereby confirming its formation. The peak fitting process involved using a combination of Gaussian and Lorentzian functions (Voigt profile) to accurately model the peak shapes, where Gaussian functions account for instrumental broadening and Lorentzian functions describe natural broadening due to the finite lifetime of the photoemission state. The fitting procedure was iteratively refined using least-squares fitting algorithms (*e.g.*, Marquardt–Levenberg or Gauss–Newton) to minimize the difference between experimental data and the fitting model. Overlapping peaks, often seen in XPS spectra due to close binding energies or multiple chemical states, were deconvoluted into individual components.[36–38] To ensure reliability, residuals were checked for randomness, and the *R*-squared and Chi-square values were monitored to confirm an optimal fit. Following deconvolution, the XPS spectra were interpreted to determine the chemical states, elemental composition, and relative concentrations of the components, providing insight into the material's chemical bonding, oxidation states, and surface composition. The low-resolution XPS survey spectra in Fig. 2(b) confirm the presence of tungsten (W), selenium (Se), carbon (C), and oxygen (O) elements on the surface of the sputtered thin film. The latter detection is in smaller quantities, potentially due to the surface oxidation of the material during the sample preparation. XPS identifies the chemical or oxidation state of the elements by analyzing shifts in the binding energies of their core electrons. Different chemical states of the same element result in distinct shifts in the binding energy of their core levels.[39] Therefore, to accurately determine the binding energies and chemical states, the C1s peak, a standard reference at 284.8 eV for carbon atoms in hydrocarbon environments, was adjusted to standardize the XPS spectra. This correction ensures precise alignment of subsequent peaks for other elements, such as W and Se, facilitating accurate analysis of their chemical environments. Fig. 2(c) presents the high-resolution XPS spectra of W4f showing the doublet peaks due to spin–orbit coupling, which splits each core level into two distinct energy levels, namely W $4f_{7/2}$, the lower energy peak in the doublet at 32.67 eV, and W $4f_{5/2}$, the higher energy peak in the doublet at 34.87 eV. In metallic tungsten, the W $4f_{7/2}$ peak is typically around 31.3 eV, and the W $4f_{5/2}$ peak is around 33.4 eV. The chemical shift obtained in the W 4f peaks shows that the tungsten is linked to selenium in its +4 oxidation state, which corresponds to W–Se bonds. The additional doublet peaks at 38.42 and 36.15 eV are likely due to the presence of an additional tungsten species or oxidation state, especially +6 (W–O bonds), which is characteristic of the WO_3 phase, likely formed due to oxidation during sample preparation.[40–42] However, Fig. 2(d) presents the high-resolution XPS spectra of Se3d. The deconvoluted spectra of selenium (Se) show a doublet due to spin–orbit coupling, corresponding to Se $3d_{5/2}$ and Se $3d_{3/2}$. The Se $3d_{5/2}$ peak appears at a lower binding energy of around 53.2 eV and the Se $3d_{3/2}$ peak appears at a higher binding energy of around 54.8 eV. Additionally, the peak at 54.69 eV corresponds to Se $3d_{5/2}$ and is consistent with values typically observed for selenium in a compound, such as in lower oxidation states of selenium found in selenium diselenide (Se_2) or selenides (Se^{2-}). The peak at 55.53 eV corresponds to the higher energy of the Se3d core level, attributed to the spin–orbit coupling.[43,44] The analysis of chemical bonding and oxidation states of the elements confirms the arrangement of W and Se in the formation of a tungsten diselenide (WSe_2) thin film.

The structural characteristics of the WSe_2 thin film were further analysed using TEM. The WSe_2 thin film was sputter deposited onto a copper TEM grid with a 300 mesh for 40 seconds, keeping other parameters the same as those discussed in Table S1.† Fig. 3(a) and (b) show the TEM images of WSe_2 at different scales providing an overview of the WSe_2 thin film morphology. The image likely shows a continuous film with well-defined nanoflakes, indicating successful deposition and uniform film formation. The contrast variation in the TEM image reveals the presence of different thickness regions within the film, with darker areas corresponding to thicker WSe_2 regions due to increased electron scattering. The HR-TEM image of WSe_2 shown in Fig. 3(c) provides atomic scale resolution, revealing the crystallinity and lattice fringes of the WSe_2 thin film.

The presence of well-defined lattice fringes in the image confirms the high crystallinity of the deposited WSe_2. The highlighted orange circles in Fig. 3(c) confirm the presence of lattice fringes in different orientations confirming the presence of different lattice planes corresponding to (103), (102), and (002) crystal planes of hexagonal WSe_2 with measured interplanar spacings of 0.24 nm, 0.26 nm, and 0.65 nm, respectively. The (103) plane represents one of the dominant planes in WSe_2, crucial for electronic properties and charge transport, the (102) plane indicates the stacking nature of WSe_2 layers, critical for maintaining stability and interlayer interactions, whereas the (002) plane corresponds to the *c*-axis stacking of WSe_2 layers, reflecting the weak van der Waals forces holding them together.[45–47] These observations confirm that the WSe_2 thin film maintains a highly ordered crystal structure, which is essential for optimizing its electronic and electrochemical performance in various applications. These obtained HR-TEM results are consistent with the XRD pattern. Elemental mapping using EDX provides spatial distribution analysis of tungsten (W) and selenium (Se) within the thin film. Fig. 3(d) shows the mixed elemental TEM mapping confirming an overlay of tungsten and selenium distribution, with a uniform elemental dispersion across the thin film, confirming the deposition process resulted in a stoichiometric and homogeneous film. Fig. 3(e) and (f) show the separate mapping of W and Se with a uniform distribution, confirming

Published on 24 2568. Downloaded on 7/6/2569 10:33:39.

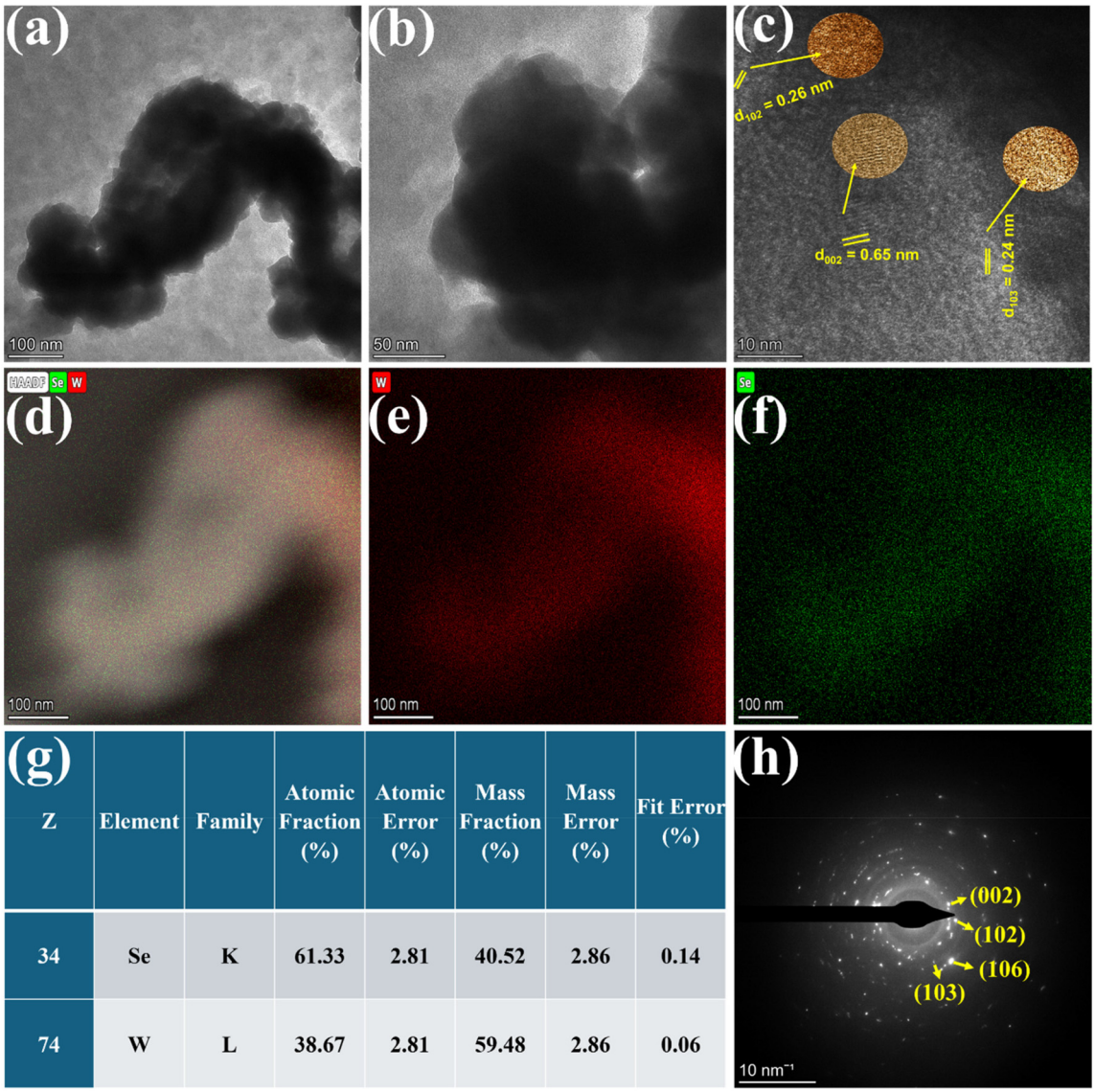

Z	Element	Family	Atomic Fraction (%)	Atomic Error (%)	Mass Fraction (%)	Mass Error (%)	Fit Error (%)
34	Se	K	61.33	2.81	40.52	2.86	0.14
74	W	L	38.67	2.81	59.48	2.86	0.06

Fig. 3 TEM images of WSe_2 at different magnifications with scale bars of (a) 100 nm and (b) 50 nm. (c) HR-TEM image with the magnified fringes in inset orange circles corresponding to different lattice planes. (d) Mixed elemental color mapping of the WSe_2 thin film. Individual elemental color mapping of (e) W and (f) Se. (g) EDX results. (h) The SAED pattern revealing different planes of WSe_2.

the absence of clustering or phase separation. A uniform and homogeneous elemental distribution is essential for ensuring uniform charge transport and electrochemical performance, particularly in energy storage applications. Any inhomogeneities could lead to localized resistance variations and performance inconsistencies. Fig. 3(g) shows the EDX results providing quantitative confirmation of the elemental composition of the WSe_2 thin film. The obtained weight percentage of EDX constituents, W ~ 38.67% and Se ~ 61.33%, confirms the synthesis of WSe_2 with the stoichiometric atomic percentage of W and Se close to the expected 1 : 2 ratio, indicating that the deposition process successfully maintained the correct stoichiometry. Deviations from this ratio may result in selenium deficiency (which could lead to structural defects) or tungsten excess (which might alter electronic properties). Fig. 3(h) shows the SAED pattern exhibiting various distinct bright spots in concentric circular rings, indicating the polycrystalline nature of the WSe_2 thin film, which confirms its hexagonal structure. The diffraction rings in the SAED pattern have been assigned to the (102), (103), (106), and (002) lattice planes, confirming the presence of 2H phases of WSe_2, which is consistent with XRD results. To evaluate the structural uniformity of the sputter-deposited WSe_2@graphite thin films, a detailed statistical analysis of crystallite size distribution and orientation was carried out using high-resolution transmission electron microscopy (HR-TEM), ImageJ software, and selected area electron diffraction (SAED). As shown in Fig. S2(a),† multiple crystallites were identified and outlined using ImageJ,

 This journal is © The Royal Society of Chemistry 2025

Published on 24 2568. Downloaded on 7/6/2569 10:33:39.

with the linear dimensions measured to estimate crystallite size. The resulting histogram (Fig. S2(b)†), generated from over six individual crystallites, demonstrates a narrow size distribution with an average crystallite size of approximately 15 ± 1 nm, indicating a homogeneous growth process and well-regulated nucleation behavior during sputtering. Complementary SAED analysis (Fig. 3(h)) revealed multiple continuous and concentric diffraction rings corresponding to the (002), (102), (103), and (106) planes of 2H-phase hexagonal WSe_2. The ring pattern confirms the polycrystalline nature of the thin films with a random crystallographic orientation, aligning with the porous, nano-cauliflower-like morphology observed in the FESEM image. The combination of uniform crystallite dimensions and random orientation signifies a structurally uniform and isotropic film. Such characteristics are beneficial for electrochemical energy storage applications, as they facilitate efficient ion transport and uniform charge distribution, ultimately enhancing the stability and performance of the supercapacitor electrodes.

3.2 Morphology and compositional analysis

The examination of surface morphology is essential for visualizing the shape, size, thickness, and distribution of a particular nanostructure obtained during the fabrication of the sputtered thin film. In this work, the morphological analysis was conducted by utilizing the Carl Zeiss Gemini300 FESEM with an operational acceleration voltage of 10 kV. The images were captured at different magnifications, specifically 5k× (5000×), 20k× (20 000×), and 150k× (150 000×), with a working distance of approximately 6 mm, as shown in Fig. 4(a–c). The top surface FESEM micrographs reveal the formation of uniformly distributed porous nano cauliflower-type surface morphology of sputtered deposited WSe_2@graphite thin films. The thickness of the thin film was adjusted in comparison to our previous studies to improve the life cycle of the created symmetric supercapacitor device, and the deposition time of 25 minutes was conducted under optimized conditions, maintaining all other parameters constant.[24,25] This change resulted in the

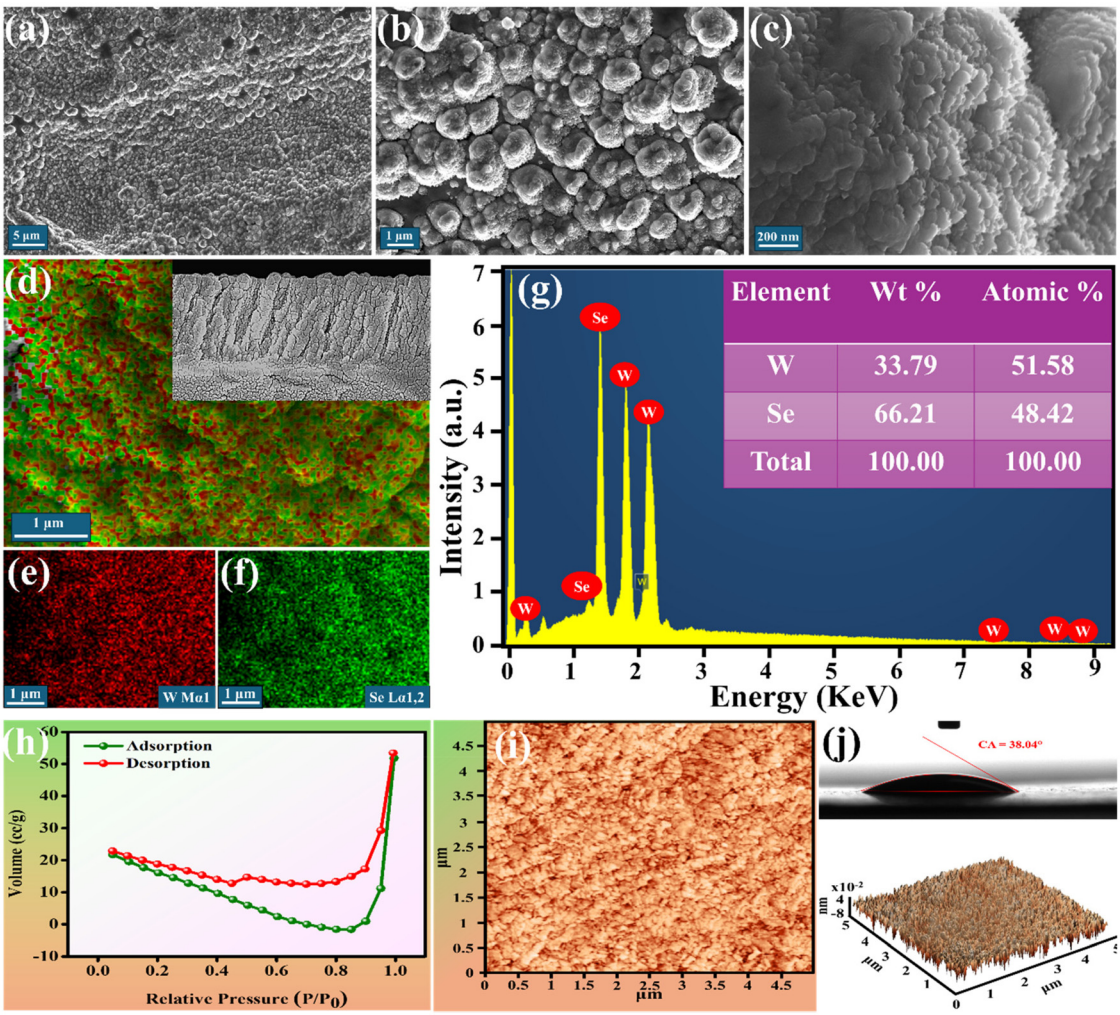

Fig. 4 FESEM images at different magnifications (a) 5k×, (b) 20k×, and (c) 150k×, (d) mixed-elemental mapping (inset: cross-sectional thickness at 50k×), individual elemental mapping of (e) W 4f and (f) Se 3d, (g) EDAX spectra, (h) BET analysis, AFM images: (i) 2D and (j) 3D of the sputtered WSe_2@graphite thin film; the inset of (j) gives contact angle measurements using the sessile drop method.

Published on 24 2568. Downloaded on 7/6/2569 10:33:39.

morphological change of the deposited thin film from nanoflakes to porous nano cauliflowers affecting the critical parameters of supercapacitors. The porous structure significantly increases the available surface area for electrochemical reactions, which leads to higher capacitance. A greater number of active sites become available for ion adsorption and desorption during charging–discharging cycles. This allows faster diffusion and transportation of ions within the material, resulting in higher charge transfer kinetics.[48–50] Furthermore, the optimized distribution of pore sizes allows effective electrolyte penetration and better accessibility to the active sites. This combination of high surface area and efficient ion transport leads to higher energy density, allowing the device to store more energy per unit area/mass/volume. The cauliflower-like structure is typically lightweight due to its porous characteristics, which further enhances energy density by minimizing the weight of the electrode material without sacrificing performance. The thickness of the fabricated thin film was determined using a cross-sectional FESEM process by placing the sample vertically under the detector. The cross-sectional micrographs were taken at a magnification of 50k× (50 000×) and a working distance of 4.3 mm. The cross-sectional FESEM shows that the thin film resulted in columnar growth with a thickness of 1.75 μm after 25 minutes with a deposition rate of 70 nm min^{-1}, as shown in the inset of Fig. 4(d). The columnar morphology is a well-known characteristic of thin films deposited *via* physical vapor deposition (PVD) techniques, such as DC sputtering. It arises from the Volmer–Weber growth mode, where spatially separated atomic nuclei form, grow, and coalesce into columnar structures due to thermodynamic and kinetic factors. The slight tilt of approximately 15° observed in our films is likely due to minor angular flux variations during sputtering, which can occur even when the target and substrate are positioned to face each other. Factors such as non-uniformity in the sputtering plume, off-axis collisions of sputtered atoms, and subtle experimental misalignments contribute to preferential shadowing effects that result in tilted columns. Additionally, the low ionization inherent to DC sputtering and the substrate temperature influence surface diffusion and further shape the columnar structure. In terms of electrochemical performance, the columnar morphology is generally beneficial, as it enhances the effective surface area, providing more active sites for charge storage or redox reactions, which are crucial for applications such as supercapacitors and batteries. The interconnected nature of the columns also facilitates ionic and electronic conductivity, enabling improved performance under high-rate conditions. Notably, it has been found that the thickness of the deposited thin film significantly impacts the electrochemical properties.[51,52] Fig. S3(a–f)† displays top-view FESEM micrographs illustrating the time-dependent surface morphological evolution of WSe_2@graphite thin films deposited by sputtering over durations ranging from 30 seconds to 30 minutes. At the shortest deposition time of 30 seconds (Fig. S3(a)†), the film surface reveals the initial nucleation of WSe_2, with early stage nanoflakes beginning to appear sporadically across the substrate. As the deposition time increases to 5 minutes (Fig. S3(b)†), these nanoflakes become more defined and distributed, indicating progressive surface coverage. A further increase to 15 minutes (Fig. S3(c)†) leads to the development of a more uniform nanoflake-based morphology. With continued deposition up to 20 minutes (Fig. S3(d)†), the nanoflakes coalesce to form a distinct, porous cauliflower-like surface architecture. At 25 minutes of deposition (Fig. S3(e)†), this cauliflower-type nanostructure becomes more pronounced, yielding a film thickness of approximately 1.75 μm. This morphology was found to be optimal for electrochemical applications, as it enhances both areal capacitance and energy density due to its high surface area and open porous structure that facilitates efficient ion transport. However, further extension of the deposition time to 30 minutes (Fig. S3(f)†) leads to morphological agglomeration, transitioning from distinct cauliflower-like structures to densely packed nanospheres, which compromise the porosity and negatively impact electrochemical performance. Fig. S3(g–i)† presents the cross-sectional FESEM images corresponding to the same deposition intervals, highlighting the evolution in film thickness and internal structural arrangement. At 30 seconds (Fig. S3(g)†), the film exhibits a minimal thickness of ~35 nm, with the initial columnar growth of nanoflakes observable. With extended deposition time, the film thickness increases to ~1.75 μm at 25 minutes (Fig. S3(h)†), showcasing vertical columnar growth consistent with the nanoflake stacking. At 30 minutes (Fig. S3(i)†), the film thickness reaches ~2.1 μm; however, this is accompanied by a loss in porosity due to agglomeration, adversely impacting ion accessibility and storage performance.

From a materials design perspective, thinner films typically offer a higher surface-area-to-volume ratio, which is advantageous for enhancing capacitance by providing more electrochemically active sites. However, overly thin films may limit ion diffusion pathways and reduce the mass of active material, thereby decreasing energy density and potentially compromising mechanical integrity during prolonged charge–discharge cycling. In contrast, thicker films can support higher energy storage due to increased active material loading but may suffer from sluggish ion transport, increased internal resistance, and structural inhomogeneity. Therefore, achieving an optimal film thickness is essential for balancing electrochemical performance parameters such as capacitance, energy density, rate capability, and mechanical stability. In this study, a sputtering duration of 25 minutes corresponding to a film thickness of approximately 1.75 μm was identified as the optimal condition. At this thickness, the porous nano-cauliflower morphology of WSe_2 provides a large electroactive surface area and open ion diffusion pathways, thereby significantly enhancing the charge storage capability of the electrode. Beyond this point, further deposition leads to reduced porosity and compromised performance due to nanostructure agglomeration.

The elemental compositions and presence of specific elements within the thin film were analyzed using the energy dispersive X-ray (EDX) spectroscopy attached to the FESEM.

 This journal is © The Royal Society of Chemistry 2025

Published on 24 2568. Downloaded on 7/6/2569 10:33:39.

Elemental mappings for WSe_2 as well as for individual elements are presented in Fig. 4(d–f), confirming the uniform distribution of tungsten (W) and selenium (Se) across the graphite surface. The quantitative EDX analysis depicted in Fig. 4(g) shows a stoichiometric ratio of W : Se::1 : 2, confirming the efficient deposition of WSe_2 onto the graphite substrate and indicating a highly pure and practically ideal composition for tungsten diselenide. The presence of an interconnected porous network enhances mechanical stability, which is essential for maintaining structural integrity during repeated cycles. This characteristic is crucial for the longevity of electrochemical devices.

3.3 Porosity and roughness analysis

The surface area and porosity of the deposited thin film were analyzed using the Brunauer–Emmett–Teller (BET) technique, which provides valuable insights into the material's porosity by differentiating between micropores (less than 2 nm), mesopores (2–50 nm), and macropores (greater than 50 nm).[53] As illustrated in Fig. 4(h), the N_2 adsorption and desorption isotherms were utilized to examine the surface morphology and texture of the material. The resulting isotherm indicates that the WSe_2@graphite thin film exhibits characteristics of both Type IV and Type VI isotherms. This observation suggests a complex porous structure characterized by mesoporosity (2–50 nm) and layered adsorption features, which can lead to non-linear adsorption behaviours. Initially, as the relative pressure approaches 0.85, a decline in the volume adsorbed is observed, dropping from 21.7 to 0 cc g^{-1}. This behavior can be attributed to the narrow and complex nature of the pores; certain pores may become filled or blocked before others, resulting in limitations in the effective adsorption area. Consequently, this situation leads to steric hindrance or repulsive interactions, wherein the existing adsorbed molecules impede the further adsorption of new molecules, thereby reducing the effective volume adsorbed. As the relative pressure rises from 0.85 to 1, an increase in adsorption volume is recorded, rising from 0 to 51.7 cc g^{-1}. This phenomenon is primarily attributed to capillary condensation; at high pressures, nitrogen molecules can condense within the pores of the material, resulting in a significant enhancement of the adsorbed gas volume. During the desorption process, as relative pressure decreases, gas molecules begin to desorb from the adsorbent surface. At elevated pressures, nitrogen molecules tend to condense within the mesopores due to capillary forces. As the pressure drops, these condensed gas molecules start to evaporate back into the gas phase, leading to a reduction in the volume of gas that can be adsorbed.[54,55] The substantial decrease in volume from 53 cc g^{-1} to 12 cc g^{-1} indicates that many gas molecules trapped in smaller pores cannot escape easily due to high capillary pressures, contributing to an initially slower desorption rate. However, as the relative pressure continues to decrease from 0.4 to 0, an increase in desorption volume is observed, rising from 12 cc g^{-1} to 22 cc g^{-1}. This increase can be attributed to the release of gas from previously inaccessible or partially blocked pores. As pressure diminishes, some of the gas trapped in narrower or more complex pore structures can escape, resulting in an apparent increase in desorbed volume, aided by the reduction of capillary forces that initially retained the gas.

This mesoporous network, with pore sizes predominantly ranging between 2 and 50 nm, plays a critical role in facilitating ion transport and storage within the electrode structure. The interplay between this pore size distribution and the ionic dimensions of the electrolytes employed, neutral Na_2SO_4, alkaline NaOH, and acidic H_2SO_4, significantly influences the electrochemical performance. The hydrated ion radius is a crucial factor governing ion accessibility to the porous electrode. The hydrated proton (H^+) from H_2SO_4, possessing an exceptionally small radius (~0.28 nm), can readily diffuse through the mesopores, maximizing active surface area utilization. Similarly, hydroxide ions (OH^-) from NaOH, with a slightly larger hydrated radius (~0.30 nm), also efficiently penetrate the porous network, facilitating enhanced charge storage interactions. Conversely, the larger hydrated ions from Na_2SO_4, sodium (Na^+, ~0.36 nm) and sulfate (SO_4^{2-}, ~0.38–0.41 nm), face steric limitations within the narrower mesopores, restricting their movement primarily to wider pores and the electrode surface. This constrained ion mobility reduces effective surface utilization and results predominantly in electric double-layer capacitance, with minimal pseudocapacitive contributions. The improved ionic mobility and pore accessibility of H^+ and OH^- ions align well with the higher capacitance and energy densities observed in acidic and alkaline electrolytes, respectively. This is further evidenced by their superior rate capability and retention at elevated scan rates and current densities, where efficient ion transport through the porous matrix is essential. In contrast, the Na_2SO_4 electrolyte, despite its excellent cycling stability, shows comparatively lower capacitance due to limited ion diffusion into smaller pores and a reliance on purely capacitive mechanisms. Therefore, the synergy between the electrode's mesoporous architecture and the size-dependent ion transport dynamics of various electrolytes critically governs the overall electrochemical behavior, balancing energy storage capacity, power delivery, and long-term stability.

The AFM analysis was conducted using Bruker's Dimension Icon instrument, and the resultant topographical data were processed with NT-MDT software to quantify surface roughness for the sputtered deposited WSe_2@graphite thin film. A sharp silicon (n-type) tip with a radius of approximately 35 nm, developed by Mikro Masch, was utilized for this analysis. The AFM was operated in non-contact mode, with the cantilever being reflective (gold-coated) to enhance detection sensitivity. The resulting 2D and 3D topography images, captured at a scale of 5 μm × 5 μm (as shown in Fig. 4(i) and (j)), reveal a notably uniform thin film morphology across the substrate. The calculated root mean square surface roughness (δ_{rms}) for the electrode is found to be approximately ~0.017 nm. These relatively low roughness values suggest a highly organized surface structure, consistent with hydrophilic behavior as outlined by the Wenzel equation.[56,57] Additionally, the wettability analysis for WSe_2@graphite thin-film electrodes

Published on 24 2568. Downloaded on 7/6/2569 10:33:39.

was conducted through contact angle measurements using the sessile drop method, as shown in the inset of Fig. 4(j). The contact angle for the WSe_2@graphite thin-film electrode was determined to be 38.02°, indicating a highly hydrophilic surface, and was found to be consistent with the AFM results. Therefore, the combined results from the AFM analysis and the contact angle measurements provide strong evidence of the hydrophilic nature of the proposed thin film, suggesting potential advantages for applications requiring enhanced surface interactions.

3.4 Electrochemical analysis

The electrochemical compatibility of WSe_2@graphite thin-film electrodes for supercapacitive applications has been well established in our previous research.[22] In this study, we expanded this investigation by exploring the influence of electrolyte pH on the electrochemical behavior of a fabricated flexible symmetric supercapacitor (FSS) device utilizing WSe_2@graphite thin-film electrodes. The FSS device was designed with these thin-film electrodes serving as both the cathode and anode. To maintain electrical neutrality and facilitate efficient ion transfer, Whatman filter paper soaked in selected aqueous electrolytes was employed as a separator, as shown in Fig. S4.† The mechanical flexibility and structural integrity of the electrodes were evaluated under various deformations, including bending, twisting, and rolling, as depicted in Fig. 5(a–e). The electrodes demonstrated remarkable resilience, retaining their original form without observable defects or degradation, thereby confirming their robust mechanical strength and flexibility. Fig. 5(f) illustrates the CV analysis of the fabricated WSe_2@graphite SS device under different bending conditions, whereas Fig. 5(g) depicts a schematic representation of the bending angles varying from 0° to 180°. The obtained CV curves remained nearly identical, with almost the same peak current and voltage window across all bending angles, indicating that the device maintains its electrochemical performance even under significant mechanical deformation. The results of electrochemical characterization further substantiate our claims regarding the mechanical flexibility and structural integrity of the electrodes and reveal it to be a promising contender for use in flexible electronic devices.

The electrochemical performance of the FSS device was evaluated using a Metrohm Autolab PGSTAT302N potentiostat/galvanostat system. In the symmetric configuration, one thin-film electrode functioned as the working electrode (WE), while the other acted as both the reference electrode (RE) and the counter electrode (CE). The assessment involved electrochemical impedance spectroscopy (EIS), cyclic voltammetry (CV), and galvanostatic charge–discharge (GCD) measurements. EIS measurements enabled a detailed assessment of the resistive and capacitive properties of the device, including internal resistance, charge-transfer resistance, and double-layer capacitance. CV provided critical insights into the charge storage behavior, while galvanostatic charge–discharge testing facilitated the determination of specific capacitance, energy density, and power density across different pH levels.

In order to explore the impact of pH, three distinct aqueous electrolytes, namely H_2SO_4 (acidic), NaOH (basic), and Na_2SO_4 (neutral), were prepared with precisely controlled concentrations, as shown in Fig. 5(h). The acidic electrolyte was prepared by dissolving 4.34 mL of H_2SO_4 in 80 mL of distilled water, while the basic electrolyte was formed by dissolving 3.2 g of NaOH in 80 mL of distilled water, and lastly, the neutral electrolyte was prepared by dissolving 11.36 g of Na_2SO_4 in 80 mL of distilled water. These specific electrolytes were selected due to their unique properties, such as ionic mobility, ion crystal radius, and Gibbs free energy, which critically influence the electrochemical processes. The ionic conductivity of electrolytes is also a key factor in determining the overall performance of the supercapacitor, as it affects the ion transport at the electrode–electrolyte interface.[58,59] The order of ionic conductivity for the three electrolytes (NaOH, H_2SO_4, and Na_2SO_4) will depend on the concentration and mobility of the ions in the solution.[60] The acidic electrolyte, sulfuric acid (H_2SO_4), dissociates into H^+ ions, resulting in a high concentration of mobile charge carriers. The H^+ ion exhibits exceptional mobility due to its small size and ability to "hop" between water molecules in the solution (known as the Grotian mechanism), making sulfuric acid a highly conductive electrolyte. The higher ionic conductivity in the electrolyte allows for more efficient ion movement and faster charge/discharge processes, thereby improving the rate capability. The high concentration of H^+ ions facilitates effective electrochemical double-layer formation at the electrode–electrolyte interface, thereby enhancing specific capacitance and increasing the electrochemical performance of the supercapacitor. In contrast, the basic electrolyte, sodium hydroxide (NaOH), dissociates to produce Na^+ and OH^- ions. Although the OH^- ion is larger than H^+, it still provides high ionic conductivity, and Na^+ ions further contribute to the conductivity. While OH^- ions are mobile, their larger size than H^+ ions results in slower transport rates, leading to reduced ion movement. Therefore, basic electrolytes typically exhibit lower ionic conductivity than acidic solutions like H_2SO_4, which can negatively affect the rate capability of the supercapacitor. Lastly, the neutral electrolyte, sodium sulfate (Na_2SO_4), dissociates to produce Na^+ and SO_4^{2-} ions. Despite its neutral pH, the ionic conductivity of Na_2SO_4 is generally lower than that of H_2SO_4 and NaOH due to the lower concentration of charge carriers, and the SO_4^{2-} ions are relatively large and less mobile compared to H^+ and OH^-. Also, the capacitance in neutral electrolytes is generally lower than in acidic and basic electrolytes because the charge storage capacity depends on ion availability at the electrode surface, and the Na_2SO_4 electrolyte does not provide as many charge carriers as its counterparts.[61]

The ionic conductivity of the prepared electrolytes was calculated by using the series resistance obtained from the EIS results, thereby supporting the above explanation. The EIS measurements were recorded over a frequency range from 0.1 Hz to 1×10^5 Hz, as seen in Fig. 5(i–k). The presence of linear features in the Nyquist plots, without the formation of a semicircle, indicates the high ionic conductivity of the prepared

 This journal is © The Royal Society of Chemistry 2025

Published on 24 2568. Downloaded on 7/6/2569 10:33:39.

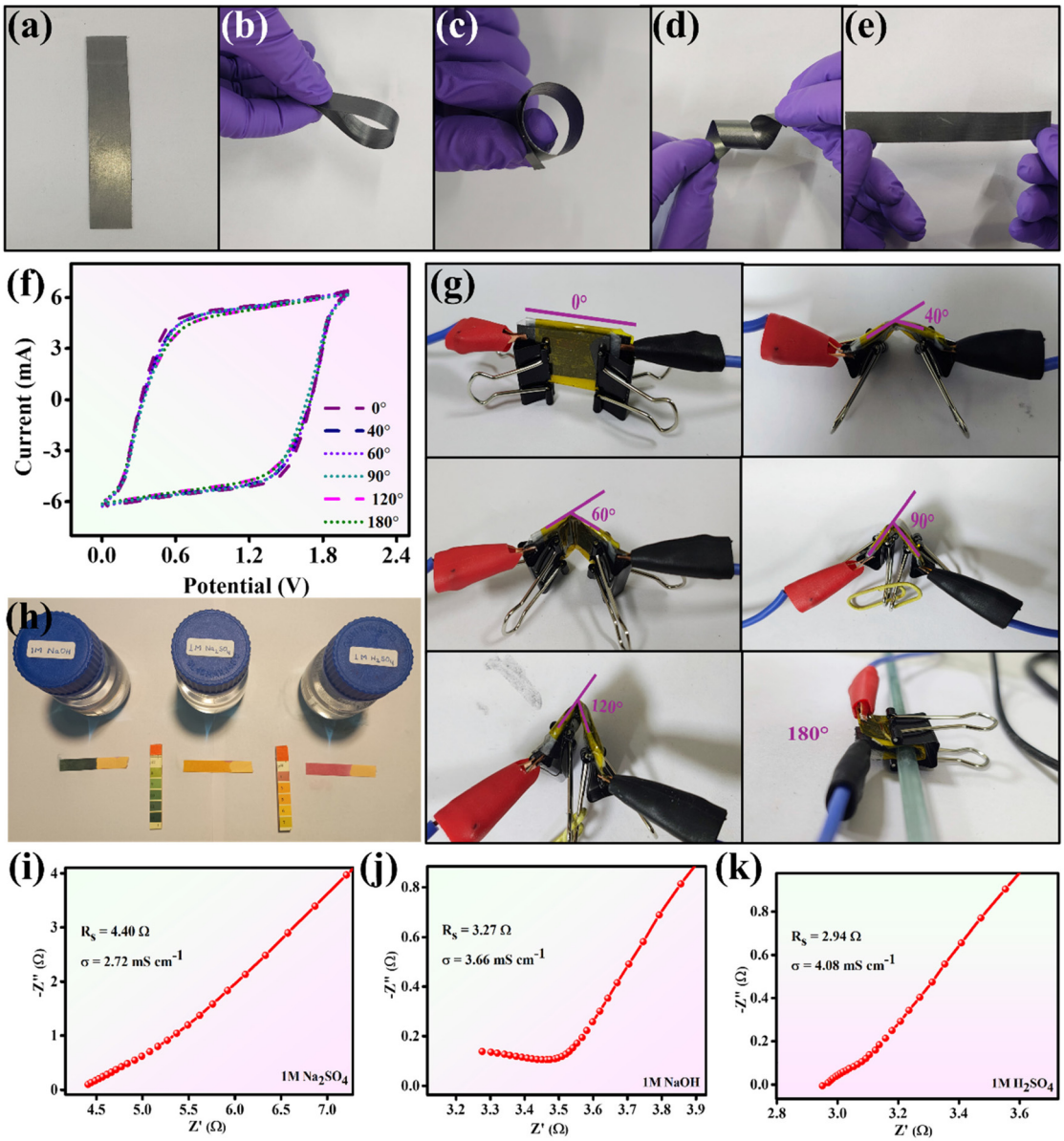

Fig. 5 Flexibility and mechanical strength test: (a) original form, (b) bent form, (c) rolled form, (d) twisted form, and (e) restoration to the initial form. (f) Electrochemical bending test from 0° to 180° at 500 mV s^{-1}, (g) WSe_2@graphite SS at different bending angles from 0° to 180°, and (h) prepared electrolytic solutions with different pH levels. EIS curves at high frequencies in different electrolytes, (i) 1 M Na_2SO_4, (j) 1 M NaOH, and (k) 1 M H_2SO_4.

electrolytic solutions. The *x*-axis intercept of the Nyquist plot provides equivalent series resistance (R_s) values. The relatively small R_s values *i.e.*, 4.40, 3.27, and 2.94 Ω for Na_2SO_4, NaOH, and H_2SO_4, respectively, indicate the excellent conductivity of the prepared electrolytes. Furthermore, eqn (1) was used to calculate the ionic conductivity of the prepared electrolytes:

$$\sigma = l/(R \times A) \quad (1)$$

where the variables σ, l, R, and A refer to the ionic conductivity in S cm^{-1}, the thickness of the electrolyte or the separator in cm (*e.g.*, the thickness of Whatman filter paper), the equivalent series resistance in Ω, and the area of the thin film electrode in cm^2, respectively. The ionic conductivity of the prepared electrolytes was found to be 2.72, 3.66, and 4.08 mS cm^{-1} for Na_2SO_4, NaOH, and H_2SO_4 electrolytes, respectively. The high ionic conductivity of the prepared electrolytes contributes to a reduction in the overall resistance of the electrochemical cell, better ion diffusion, and higher capacitance, and hence the superior power performance of the SS device.

In order to explore the supercapacitive performance and the impact of the pH levels of different aqueous electrolytes on the electrochemical performance, a symmetric supercapacitor device was fabricated using WSe_2@graphite thin film electro-

Published on 24 2568. Downloaded on 7/6/2569 10:33:39.

des functioning as both the cathode and the anode with a Whatman filter paper soaked in the electrolytic solution and sandwiched in between these electrodes. The electrochemical assessment was performed utilizing CV, GCD, and EIS techniques. Fig. 6(a–c) shows the CV curves recorded at different scan rates from 50 to 1500 mV s^{-1} in different aqueous electrolytes with distinct pH levels. The resulting CV curves help to understand the behavior of the fabricated SS. Fig. 6(a) shows the CV curves at different scan rates in the Na_2SO_4 electrolyte, which has a neutral pH value of approximately 7. The neutral pH minimizes faradaic processes, resulting in pure EDLC behavior. The absence of pH-induced redox reactions ensures long-term electrode stability but offers limited energy density. The rectangular shape of the CV curves at low scan rates indicates the ideal double-layer capacitive behavior, which is characteristic of the systems where the charge is stored through ion adsorption at the electrode–electrolyte interface. At higher scan rates, the CV curves begin to deviate from the rectangular shape due to increasing resistive (IR) losses and incomplete ion interactions, which are prevalent at faster rates.

Fig. 6(b) shows the CV curves at different scan speeds with a NaOH electrolyte with a basic pH value of approximately 14. The alkaline pH environment enhances the pseudocapacitive behavior through redox reactions that involve OH^- ions. However, prolonged exposure to high pH levels can corrode electrode materials. The energy density was found to be higher than Na_2SO_4 due to additional pseudocapacitive contributions. The current response in NaOH surpasses that in Na_2SO_4 at the same scan rates due to the contribution of the pseudo-capacitance from faradaic redox reactions involving OH^- ions. At lower scan rates, distinct redox peaks are visible, representing reversible oxidation–reduction processes. These peaks tend to diminish or broaden at higher scan rates due to kinetic limitations. The presence of redox peaks at lower scan rates indicates the pseudocapacitive behavior, where charge storage occurs through faradaic processes in addition to the double-layer effects. At higher scan rates, limitations in ion diffusion and reaction kinetics result in reduced visibility of redox activity. Fig. 6(c) shows the CV curves at different scan speeds in the H_2SO_4 electrolyte, demonstrating the behavior with acidic pH. The acidic pH enables strong pseudocapacitive behavior due to H^+ ions participating in the redox reactions, resulting in the highest areal capacitance and energy density. The curve shows highly symmetric redox peaks at lower scan rates, although the overall shape deviates from the rectangular form. The dominance of redox peaks is attributed to the strong pseudocapacitive behavior involving H^+ ions and reversible reactions. The acidic environment enables efficient ion transport and fast redox processes; however, kinetic limitations become apparent at high scan rates. All these aqueous electrolytes demonstrate a broad electrochemical potential window of 2 V, ranging from 0 to +2 V, indicating the extraordinary performance of the fabricated SS. The areal capacitance and corresponding energy densities from the CV analysis were calculated using eqn (ES1) and (ES2),† respectively. The calculated values of areal capacitance and corresponding energy densities at increasing scan speeds in different electrolytes are detailed in Tables S2–S4.† From the results, it has been observed that as the scan rate increases, both areal capacitance

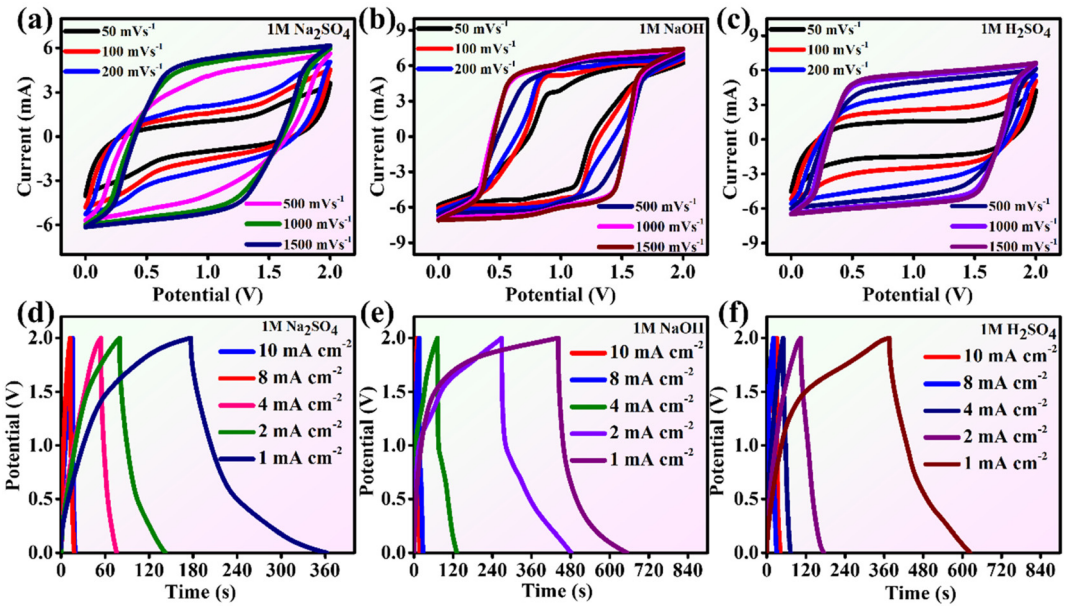

Fig. 6 Cyclic voltammetry curves at different scan rates *i.e.*, 50 to 1500 mV s^{-1} in different aqueous electrolytes: (a) 1 M Na_2SO_4 with a neutral pH level, (b) 1 M NaOH with a basic pH level, and (c) 1 M H_2SO_4 with an acidic pH level. Galvanostatic charge–discharge curves at different current densities *i.e.*, 1 to 10 mA cm^{-2} in different aqueous electrolytes: (d) 1 M Na_2SO_4 with a neutral pH level, (e) 1 M NaOH with a basic pH level, and (f) 1 M H_2SO_4 with an acidic pH level.

This journal is © The Royal Society of Chemistry 2025

Published on 24 2568. Downloaded on 7/6/2569 10:33:39.

and energy density decrease. At low scan rates, ions have sufficient time to access the porous electrode structure, maximizing charge storage. While at high scan rates, only the outer electrode surface is accessed, resulting in reduced effective capacitance. This behavior is attributed to the difficulties associated with electrolyte ion diffusion on the electrode surface at higher scan rates; the rapid changes in potential do not provide sufficient time for ions to interact effectively with the electrode surface, leaving the inner surfaces of the pores inaccessible for interaction. Fig. 6(d–f) depicts the typical charge–discharge curves at several current densities varying from 1 to 10 mA cm^{-2} across different electrolytes. The resulting GCD curves help in further understanding the electrochemical behavior of the fabricated SS. The characteristics of the GCD curves directly affect areal capacitance and energy density because these properties depend on the discharge time, symmetry, and the type of charge-storage mechanism, whether capacitive or pseudocapacitive. Fig. 6(d) shows the GCD curves at different current densities in a neutral electrolyte (Na_2SO_4). The curve exhibits a symmetric and nearly linear profile, representing the ideal capacitive behavior characteristics of an electric double-layer capacitor (EDLC). These characteristics indicate that charge storage occurs primarily through physical adsorption/desorption of ions at the electrode interface, with no significant faradaic (redox) reactions taking place due to the neutrality of the electrolyte. In comparison with acidic or basic electrolytes, discharge times are shorter since the capacitance relies solely on physical mechanisms, without the influence of faradaic reactions. The neutral pH level contributes to stability, no redox contributions, and consistent charge–discharge behavior. Fig. 6(e) shows the GCD curve in a NaOH electrolyte at an alkaline pH level. The GCD curve is less symmetric and exhibits nonlinearity when compared to Na_2SO_4. This behavior arises due to the faradaic reactions involving OH^- ions to the charge storage. The pseudocapacitive characteristics of NaOH lead to nonlinear profiles, while the incomplete reversibility of faradaic reactions results in asymmetric behavior. Fig. 6(f) shows the GCD curve in an acidic electrolyte (H_2SO_4). In this instance, the GCD curve exhibits greater symmetry and linearity compared to NaOH, despite significant pseudocapacitive contributions. This observation indicated that the faradaic processes in an acidic environment are highly reversible and efficient. The small and highly mobile H^+ ions facilitate fast and uniform charge transfer, thereby minimizing distortions in the curve. The areal capacitance with corresponding areal energy density and power density of the SS device were determined from the GCD curves using eqn (ES3)–(ES5),† providing more precise insights into the electrochemical performance, and the obtained results are tabulated in Tables S5–S7.†

As we know, EIS is a crucial technique for understanding the charge storage and ion transport mechanism in supercapacitors. EIS analysis conducted within the frequency range of 0.1 to 1×10^5 Hz provides a detailed evaluation of electrochemical performance across various electrolytes. Fig. 7(a) shows the Nyquist plot of the FSS device in electrolytes exhibiting varying pH values. The Nyquist plot derived from the neutral electrolyte (Na_2SO_4) displays a nearly linear profile throughout the frequency range, with no noticeable semicircle at high frequencies. The linearity indicates ideal capacitive behaviour, consistent with the electric double-layer capacitance (EDLC). In such configurations, the impedance is primarily dominated by capacitive contributions rather than resistive or faradaic components. The absence of a semicircle at higher frequencies suggests minimal charge-transfer resistance, implying no significant pseudocapacitive redox reactions.[62,63] The steep slope in the low-frequency region indicates efficient ion diffusion within the electrolyte and towards the electrode surface, thereby ensuring optimal capacitive performance. The neutral pH level prevents faradaic processes, resulting in stable and reversible charge storage dominated by ion adsorption/desorption. While Na_2SO_4 provides a stable electrolyte environment, its lack of pseudocapacitive contributions limits the overall capacitance. The electrolyte is particularly suitable for applications where long-term stability is prioritized over high-energy storage. Therefore, the alkaline electrolyte (NaOH) shows a semicircular region at higher frequencies, transitioning to a linear region at lower frequencies. The semicircle observed at higher frequencies reflects charge-transfer resistance (R_{ct}), which arises from redox reactions at the electrode interface, resulting in the pseudocapacitive behavior of the system. The linear region observed at lower frequencies indicates capacitive behavior, but the deviation from ideality suggests mixed contributions from both EDLC and pseudocapacitance.[64,65] The presence of R_{ct} suggests that the kinetics of charge transfer are slower in comparison with Na_2SO_4, likely due to the involvement of OH^- ions in faradaic reactions. However, the transition to linear behavior indicates that ion diffusion remains reasonably efficient at lower frequencies. The alkaline medium promotes redox reactions involving OH^- ions, enhancing the overall capacitance through pseudocapacitive contributions. However, these reactions introduce resistance, thereby reducing charge/discharge rates at higher frequencies. NaOH offers a balance between capacitance and resistance, with a higher energy storage potential compared to Na_2SO_4 due to pseudocapacitance. However, its performance may be limited at very high frequencies due to charge-transfer resistance. In the case of the acidic electrolyte (H_2SO_4), the Nyquist plot shows deviation from linearity at higher frequencies, indicating a smaller semicircular feature, followed by a nearly linear trend at lower frequencies. The small semicircular region reflects moderate R_{ct}, indicating some redox reactions occurring at the electrode interface. These reactions contribute to pseudocapacitive behavior, albeit to a lesser extent than NaOH. The near-linear behavior at lower frequencies suggests that EDL formation remains predominant, although with a less ideal capacitive response compared to Na_2SO_4. The relatively small semicircle indicates efficient charge transfer compared to NaOH, but the deviation from linearity suggests that ion diffusion is slightly hindered at high frequencies. The acidic medium enhances H^+ ion mobility, facilitating fast charge/discharge processes and pseudocapacitive reactions. However, the strong acidity may also lead to degradation of the electrode material, potentially affecting long-term performance. The EIS analysis

Published on 24 2568. Downloaded on 7/6/2569 10:33:39.

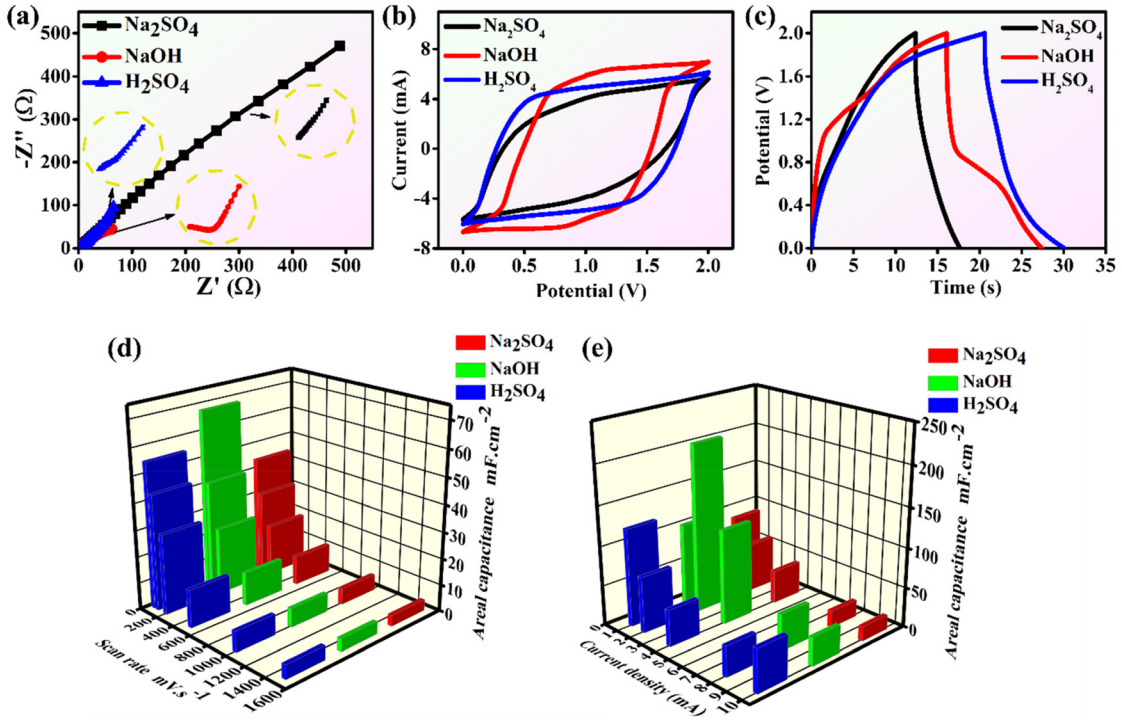

Fig. 7 Electrochemical performance of the WSe_2@graphite thin film electrode in different electrolytes exhibiting varying pH levels: (a) Nyquist plot with an enlarged view of the high frequency in the inset circles, (b) cyclic voltammetry curves at a scan speed of 500 mV s^{-1}, (c) galvanostatic charge–discharge curves at a current density of 8 mA cm^{-2}, (d) comparison of areal capacitance with an increase in scan rates (50–1500 mV s^{-1}), and (e) comparison of areal capacitance with an increase in current densities ranging from 1 to 10 mA cm^{-2}.

conducted through EIS confirms that H_2SO_4 provides the best trade-off between high capacitance (*via* pseudocapacitance) and low resistance, which makes it ideal for applications requiring both high energy and power densities. However, electrode stability under acidic conditions must be carefully managed. Fig. 7(b) displays the comparative CV curves in different electrolytes at a scan speed of 500 mV s^{-1}. The area enclosed by each CV curve corresponds to the charge storage capability of the electrode material within the given electrolyte. A large, enclosed area indicates a higher current at each potential, implying higher charge storage capacity. Among the examined electrolytes, the CV curve of Na_2SO_4, a neutral electrolyte with restricted ionic conductivity, exhibits the smallest enclosed area. In contrast, the CV curve of H_2SO_4, an acidic electrolyte, shows the largest area among the three tested electrolytes. Fig. 7(c) presents comparative GCD plots in different electrolytes at a current density of 8 mA cm^{-2}. The symmetry, slope, and duration of the GCD curve directly affect the electrochemical parameter.[66,67] Symmetric charge–discharge profiles typically suggest ideal capacitive behavior, indicating efficient energy storage. Any asymmetry may indicate resistive loss or additional faradaic processes. Steeper curves indicate rapid charging/discharging, usually associated with high conductivity of the electrolyte. Longer discharge times at the same current density suggest higher capacitance. The GCD curve corresponding to Na_2SO_4 (neutral electrolyte) shows symmetric triangular shapes, indicating pure electric double-layer capacitance (EDLC) behavior. Discharge time is comparatively shorter than that of NaOH and H_2SO_4, indicating a lower areal capacitance and energy storage capacity. In the case of NaOH (alkaline electrolyte), the curve is slightly steeper during charging and discharging compared to Na_2SO_4, showing faster ion transport kinetics. Discharge time is moderately longer, reflecting higher areal capacitance due to improved ionic conductivity and partial pseudocapacitive behavior at the electrode interface. However, the acidic electrolyte (H_2SO_4) demonstrates the longest discharge time, reflecting the highest areal capacitance among the three electrolytes. The shape of the curve may exhibit subtle asymmetry, suggesting additional faradaic contributions beyond EDLC. The strong ionic strength and high proton conductivity in H_2SO_4 enable efficient charge storage and delivery. The GCD curves indicate that the H_2SO_4 outperforms the other electrolytes in terms of areal capacitance and energy density, while NaOH provides moderate performance due to enhanced ionic mobility. Conversely, Na_2SO_4 is the least effective, offering pure EDLC behavior with limited ionic conductivity. Fig. 7(d) illustrates the effects of areal capacitance on scan rates in various electrolytes. In the case of the neutral Na_2SO_4 aqueous electrolyte, the areal capacitance decreases from 44 mF cm^{-2} at 50 mV s^{-1} to 4.19 mF cm^{-2} at 1500 mV s^{-1}. The decrease in capacitance with an increase in the scan rate is typical of capacitive materials because, at higher scan rates, there is less time for ions to diffuse into the electrode surface, leading to lower charge storage. However, for the basic NaOH electrolytes, initial areal capacitance is higher than Na_2SO_4 (67.9 mF cm^{-2} at 50 mV s^{-1}), but it

 This journal is © The Royal Society of Chemistry 2025

Published on 24 2568. Downloaded on 7/6/2569 10:33:39.

also decreases significantly with an increase in the scan rate. Basic electrolytes typically enhance the adsorption of OH^- ions at the electrode surface, potentially increasing capacitance at lower scan rates. However, at higher scan rates, the limited ion diffusion leads to a reduction in capacitance at faster charging/discharging rates. In the case of acidic H_2SO_4 electrolytes, areal capacitance is observed to be lower than NaOH at 50 mV s^{-1} (54.92 mF cm^{-2}); however, the decline in capacitance with an increase in the scan rate is more gradual. In acidic electrolytes, H^+ ions are highly mobile and can easily diffuse into the electrode surface, leading to higher capacitance and better performance at higher scan rates compared to neutral or basic electrolytes. The energy density (E_a) follows a similar trend to areal capacitance, although it is typically lower due to the relationship between the voltage window and capacitance. For neutral electrolytes (Na_2SO_4) the energy density decreases from 24.4 μF cm^{-2} at 50 mV s^{-1} to 2.32 μF cm^{-2} at 1500 mV s^{-1}. The reduction in the energy density is attributed to the diminished capacity of ions to interact with the electrode surface at higher scan rates. For the basic electrolyte (NaOH), the energy density shows a higher value than that of Na_2SO_4 at all scan rates, reaching 37.75 μF cm^{-2} at 50 mV s^{-1}. This may be due to the smaller size of OH^- ions compared to SO_4^{2-} ions, enabling faster ion movement and greater capacitance at low scan rates, translating into a higher energy density. However, for acidic electrolytes (H_2SO_4) the energy density also shows a high value but lower than that of NaOH. At 50 mV s^{-1}, it approaches 30.51 μF cm^{-2}. The H^+ ions offer high ionic conductivity, leading to good energy density at lower scan rates, but not as high as NaOH due to the lower ionic charge density compared to OH^-. Fig. 7(e) shows the comparison of areal capacitance with an increase in the current density from 1 to 10 mA cm^{-2} for various electrolytes. For the Na_2SO_4 electrolyte with a neutral pH level, the areal capacitance decreases with an increase in the current density *i.e.* 92.92, 62.26, 41.85, 21.32, and 18.23 mF cm^{-2} for 1, 2, 4, 8, and 10 mA cm^{-2}, respectively. This behavior occurs because, at low current densities, ions have more time to diffuse into the electrode pores and form a robust electric double layer (EDL), thereby maximizing charge storage. Whereas, at higher current densities, the time for ion diffusion is limited, and only the outer surface of the electrode contributes to charge storage, resulting in lower capacitance. On the other hand, the alkaline electrolyte, NaOH, exhibits an irregular trend of areal capacitance with values of 105.71, 212.73, 119.25, 45.66, and 34.95 mF cm^{-2} at the corresponding current densities of 1, 2, 4, 8, and 10 mA cm^{-2}, respectively. The higher initial capacitance at low current densities is due to the enhanced pseudocapacitive behavior from redox reactions involving OH^- ions (*e.g.*, surface oxidation/reduction of the WSe_2@graphite). The anomalously high capacitance at 2 mA cm^{-2} suggests optimized redox activity and EDL formation at this specific current density. As current densities increase, the contribution of redox reactions diminishes due to kinetic limitations, leading to a drop in capacitance. The acidic electrolyte, H_2SO_4, exhibits a varying trend of areal capacitance with values of 123.73, 71.01, 46.09, 37.70, and 53.72 mF cm^{-2} at current densities of 1, 2, 4, 8, and 10 mA cm^{-2}, respectively. The high initial capacitance is attributed to the strong pseudocapacitive behavior involving H^+ ions and their efficient penetration into the electrode. The dip at intermediate current densities suggests the presence of kinetic or mass transport limitations. The increase in capacitance at higher current densities (10 mA cm^{-2}) may result from enhanced redox activity or improved electrode utilization at high rates. The energy and power density are two crucial factors for evaluating the supercapacitive performance. Since the energy density is directly proportional to the areal capacitance, the energy density follows a similar trend. However, power density increases with an increase in the current density and remains consistent across all electrolytes, which is highly beneficial for the symmetric supercapacitor device as shown in Tables S5–S7.† This information aids in the selection of an appropriate electrolyte providing the best areal capacitance and energy density while maintaining the power density of the device.

Table 1 presents a comparison of the electrochemical performance metrics of the WSe_2@graphite thin-film electrode, including its potential window, areal capacitance, energy density, and power density, with those of previously reported TMDC-based electrode materials.[18,68–77] The results demonstrate that the symmetric supercapacitor device fabricated using the WSe_2@graphite composite exhibits superior performance, characterized by a wide potential window of 2 V and significantly enhanced areal capacitance, energy, and power densities.

These findings highlight the exceptional capabilities of the WSe_2@graphite composite as a flexible electrode material for SS applications. Moreover, the device's adaptability across various pH environments and the ability to select electrolytes based on the optimal balance of energy, power, and stability underscore its potential for advanced energy storage systems.

Furthermore, we have analyzed the cycling stability of the fabricated SS device across various electrolytes, executing 5000 GCD cycles at a current density of 8 mA cm^{-2} within a potential window of 0 to +2 V. Fig. 8(a–c) illustrates the cycling stability plots in terms of % cyclic retention *versus* the number of cycles in different electrolytes. The insets of Fig. 8(a–c) present the GCD curves before and after 5000 GCD cycles for Na_2SO_4, NaOH, and H_2SO_4 electrolytes. Among these electrolytes, Na_2SO_4 exhibits the highest cyclic retention ratio of 92.5%, followed by 86.3% in NaOH, and 78.69% in H_2SO_4 after 5000 GCD cycles. The cycling stability of the WSe_2@graphite-based symmetric supercapacitor can be attributed to the chemical characteristics and their interactions with the electrode materials. In the case of Na_2SO_4, the chemically stable environment minimizes aggressive chemical reactions, allowing for primarily electric double-layer capacitance mechanisms, which impose minimal stress on WSe_2 and graphite materials. This results in superior stability as the degradation from side reactions or structural changes is negligible. In the case of NaOH, the alkaline environment introduces hydroxyl ions (OH^-), which may participate in partial faradaic reactions with the electrode surfaces, leading to the formation of surface oxides and potential degradation of the electrode over extended cycling. The higher ionic conductivity of NaOH initially

Published on 24 2568. Downloaded on 7/6/2569 10:33:39.

Table 1 Comparison of the performance parameters of the fabricated WSe_2@graphite thin film electrode with various previously reported literature data

S. no.	Electrode material	Electrolyte	Synthesis method	Potential window (V)	Areal capacitance (mF cm^{-2})	Energy density (mWh cm^{-2})	Power density (mW cm^{-2})	Ref.
1.	MoS_2@CNT/RGO	1 M H_2SO_4	Simple vacuum-assisted filtration method	1	29.5	0.00413	3.2	68
2.	$MoSe_2$ solid-state supercapacitor	Ionogel electrolyte	Hydrothermal method	2	18.93	37.9 mJ cm^{-2}	0.268	69
3.	MoS_2	0.5 M H_2SO_4	RF magnetron sputtering	0.2	33	0.000233	8	70
4.	WSe_2@graphite	1 M Na_2SO_4	DC sputtering	1.1	3.91	0.00782	0.598	18
5.	W-doped $MoSe_2$/ graphene	PVA/KOH	One-step hydrothermal catalysis	0.9	60.5	3	150	71
6.	Metallic 1T-WS_2 nanoribbons	1 M H_2SO_4	Hydrothermal synthesis	1	2.813	—	—	72
7.	WS_2 quantum dots	H_3PO_4-PVA	Hydrothermal route	0.6	28	1.49	47.03	73
8.	AgNWs–MoS_2	1 M PVA-H_2SO_4	Electrochemical polymerization and film transfer methods	1.2	27.6	0.00245	1.472	74
9.	MoS_2@$Ni(OH)_2$	PVA/KOH	Single-mode microwave hydrothermal technique	1	14.07	0.52	1.1	75
10.	MoS_2/rGO/CNT	1 M Na_2SO_4	Electroactive coating	1	93.2	0.0129	1.96	76
11.	h-WO_3/WS_2 nanowire	Na_2SO_4 (0.1 M)	CVD	0.8	18.3	0.06 Wh cm^{-3}	—	77
12.	WSe_2@graphite SS	1 M Na_2SO_4	DC sputtering	2	92.92	0.0516	1	This work
13.	WSe_2@graphite SS	1 M NaOH	DC sputtering	2	105.71	0.0587	1	This work
14.	WSe_2@graphite SS	1 M H_2SO_4	DC sputtering	2	123.73	0.0687	1	This work

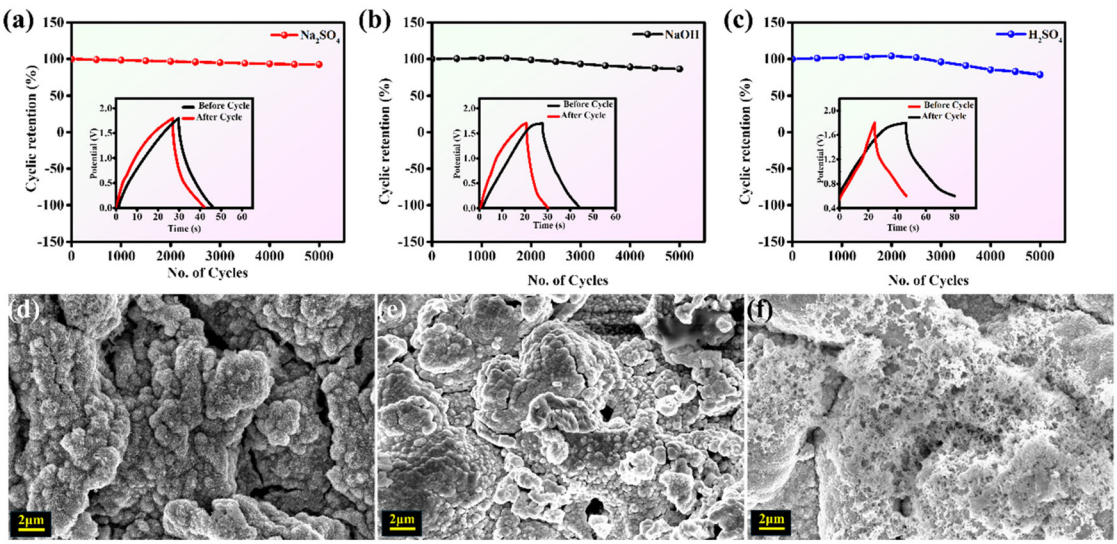

Fig. 8 (a) Cycling stability curve with the inset showing the first and last GCD cycles at 8 mA cm^{-2}, and the corresponding FESEM images of the WSe_2@graphite electrode after 5000 cycles with different electrolytes: (a and d) Na_2SO_4, (b and e) NaOH, and (c and f) H_2SO_4.

enhances performance but accelerates material deterioration over time due to electrochemical stress. In contrast, H_2SO_4, being a strongly acidic electrolyte, creates a highly corrosive environment where protons (H^+) and sulfate ions (SO_4^{2-}) actively interact with WSe_2 and graphite, resulting in material corrosion and weakening of structural integrity. The acidic conditions also promote extensive faradaic reactions, leading to enhanced initial capacitance, resulting in significant electrode degradation and capacity fading over repeated cycles. Therefore, the highest cycling stability in Na_2SO_4 is due to its neutral, non-aggressive nature, while the progressively lower stability in NaOH and H_2SO_4 stems from their increasing reactivity and corrosive effects on the electrode materials.

Fig. 8(d–f) show the FESEM images of the WSe_2@graphite symmetric supercapacitor device examined after 5000 GCD cycles. Before the GCD cycles, the WSe_2@graphite pristine thin film displays a uniform and well-structured morphology. The film exhibits tightly packed layers with minimal surface irregularities, indicating its structural integrity. This morphology ensures a high surface area for electrolyte interaction, which is highly beneficial for electrochemical properties. However, Fig. 8(d) shows the FESEM image after 5000 GCD cycles with

 This journal is © The Royal Society of Chemistry 2025

Published on 24 2568. Downloaded on 7/6/2569 10:33:39.

Na_2SO_4 showing minimal morphological degradations. The structure largely retains its original uniformity, with only slight indications of wear. This stability is attributed to the neutral nature of Na_2SO_4, which avoids aggressive chemical reactions with the electrode material. The absence of corrosive ions (*e.g.*, H^+ or OH^-) limits chemical degradation, preserving the integrity of the WSe_2@graphite surface. This explains the high cycling stability (92.5%) in Na_2SO_4. Additionally, Fig. 8(e) shows the FESEM image obtained after 5000 GCD cycles with NaOH, and the alkaline environment introduces hydroxyl ions (OH^-), leading to visible morphological degradation in certain regions on the material surface. These changes may include localized peeling, roughening, or formation of surface oxides. The degradation is attributed to the chemical reactions between OH^- and the electrode material, which can form surface oxides or hydroxides, altering the material's structure. The degradation is moderate and shows a cycling stability of around 86.3%. Moreover, Fig. 8(f) shows the FESEM image after 5000 cycles with H_2SO_4 revealing significant destruction of the material surface, with most of the surface covered by the electrolyte or completely degraded. The acidic environment introduces highly reactive protons (H^+) and sulfate ions (SO_4^{2-}), which corrode the WSe_2 and graphite surface. This leads to the breakdown of the electrode's structural integrity, loss of active material, and formation of non-conductive surface layers. The aggressive interaction with the electrolyte results in poor cycling stability of approximately 78.69%.

In summary, we have successfully fabricated a highly porous and flexible symmetric supercapacitor device based on WSe_2@graphite. This device underwent treatment with different aqueous electrolytes, acidic, basic, and neutral, to investigate the impact of pH levels on the fabricated SS device. The device resulted in an extraordinary potential window of 2 V (0 to +2 V) across all three electrolytic solutions, highlighting its adaptability and extraordinary stability over distinct pH levels. Acidic electrolytes resulted in the best performance in terms of capacitance, rate capability, and electrochemical efficiency due to their high ionic conductivity and favourable charge storage dynamics. However, the strong acidity also limited the long-term stability compared to the other electrolytes. Sodium sulfate (Na_2SO_4), as a neutral electrolyte, exhibited the lowest conductivity and capacitance due to its neutral pH, which minimizes faradaic processes and results in pure electric double-layer capacitance. This electrolyte ensures excellent long-term stability by preventing aggressive chemical reactions with electrode materials. In the end, sodium hydroxide (NaOH), with its basic pH level, supports pseudocapacitance through redox reactions involving OH^- ions. Although it offers moderate ionic conductivity and capacitance, the larger size of its ion reduces transport efficiency compared to H^+, and the alkaline conditions can corrode electrodes over time. Therefore, the electrochemical assessments, including CV, GCD, and EIS, reveal that H_2SO_4 offers superior energy and power density due to its efficient redox processes. In contrast, NaOH demonstrates moderate performance, while Na_2SO_4 excels in stability but lacks in energy density. Ultimately, the selection of electrolytes depends upon the desired trade-off between energy, power, and stability.

4 Conclusion

In summary, a cost-effective and lithography-free approach has been utilized for the successful fabrication of hierarchical nanocomposite flexible symmetric supercapacitor electrodes based on WSe_2@graphite thin films. This device underwent treatment with different aqueous electrolytes including acidic, basic, and neutral to investigate the impact of different pH levels on the supercapacitive performance of the fabricated SS device. The resulting device exhibits an extraordinary potential window of 2 V (0 to +2 V) across all three electrolytic solutions with high adaptability and stability over distinct pH levels. Furthermore, the findings indicate a significant influence of pH levels on the supercapacitive properties of the WSe_2@graphite-based SS device. Acidic electrolytes offer the best supercapacitive properties in terms of capacitance, rate capability, electrochemical efficiency, and energy and power density with moderate long-term stability compared to the other electrolytes. Neutral electrolytes exhibit the lowest conductivity, capacitance, and energy density due to their minimal faradaic processes but offer excellent long-term stability. Lastly, basic electrolytes offer moderate ionic conductivity and capacitance in comparison with other electrolytes. Therefore, electrochemical assessments reveal that the acidic electrolyte (H_2SO_4) offers superior supercapacitive properties including ionic conductivity (4.08 mS cm^{-1}) and areal capacitance (123.73 mF cm^{-2}) with the corresponding energy density (68.73 μWh cm^{-2}) and power density (1000 μW cm^{-2}) at a current density of 1 mA cm^{-2}. Ultimately, these findings favour the promising potential of the flexible WSe_2@graphite composite as the electrode material for symmetric supercapacitor applications under different pH conditions, with the choice of electrolyte based on the desired trade-off between energy, power, and stability.

Author contributions

Akshay Tomar: conceptualization, visualization, investigation, methodology, data curation, and writing – original draft. Nitesh Choudhary: investigation, methodology, and writing – review and editing. Radhika Jain: writing – review and editing and data curation. Dushyant Chaudhary: writing – review and editing. Gaurav Malik: visualization, data curation, and writing – review. Sheetal Issar: writing – review and editing and data curation. Ramesh Chandra: supervision, project administration, validation, and resources.

Conflicts of interest

The authors declare no competing financial interest.

Published on 24 2568. Downloaded on 7/6/2569 10:33:39.

Data availability

The authors confirm that the data supporting the findings of this study are available within the article and its ESI.† The data will also be made available on request.

Acknowledgements

Akshay Tomar would like to express his gratitude to the Ministry of Education (MoE) and IIT Roorkee for funding the research fellowship. The authors acknowledge the DST for supporting the present work through project no. DST/TMD/MES/2k18/36.

References

1 A. M. Adeyinka, O. C. Esan, A. O. Ijaola and P. K. Farayibi, *Sustain. Energy Res.*, 2024, **11**, 26.
2 J. Zhang, M. Gu and X. Chen, *Micro Nano Eng.*, 2023, **21**, 100229.
3 Y. A. Kumar, N. Roy, T. Ramachandran, M. Hussien, M. Moniruzzaman and S. W. Joo, *J. Energy Storage*, 2024, **98**, 113040.
4 V. Manisha, P. Tonya and J. Li, *J. Energy Eng.*, 2013, **139**, 72–79.
5 N. Kurra and Q. Jiang, in *Storing Energy*, ed. T. M. Letcher, Elsevier, 2nd edn, 2022, pp. 383–417.
6 N. Choudhary, S. Singh, S. Bhardwaj, S. Gupta, U. Nandi, R. Chandra and P. K. Maji, *Carbohydr. Polym. Technol. Appl.*, 2024, **7**, 100416.
7 X. He and X. Zhang, *J. Energy Storage*, 2022, **56**, 106023.
8 K. S. Ngai, in *Encyclopedia of Energy Storage*, ed. L. F. Cabeza, Elsevier, Oxford, 2022, pp. 341–350.
9 A. Aggarwal, I. M. Allafi, E. G. Strangas and J. S. Agapiou, *IEEE Trans. Transp. Electrif.*, 2021, **7**, 161–169.
10 A. A. Tedstone, D. J. Lewis and P. O'Brien, *Chem. Mater.*, 2016, **28**, 1965–1974.
11 D. Monga, S. Sharma, N. P. Shetti, S. Basu, K. R. Reddy and T. M. Aminabhavi, *Mater. Today Chem.*, 2021, **19**, 100399.
12 S. Manzeli, D. Ovchinnikov, D. Pasquier, O. V. Yazyev and A. Kis, *Nat. Rev. Mater.*, 2017, **2**, 17033.
13 J. Cherusseri, N. Choudhary, K. Sambath Kumar, Y. Jung and J. Thomas, *Nanoscale Horiz.*, 2019, **4**, 840–858.
14 J. Li, S. Han, J. Zhang, J. Xiang, X. Zhu, P. Liu, X. Li, C. Feng, B. Xiang and M. Gu, *J. Mater. Chem. A*, 2019, **7**, 19898–19908.
15 J. H. Nam, M. J. Jang, H. Y. Jang, W. Park, X. Wang, S. M. Choi and B. Cho, *J. Energy Chem.*, 2020, **47**, 107–111.
16 A. Tomar, S. Issar, R. Adalati and R. Chandra, *ECS Meeting Abstracts*, 2023, MA2023-02, 3247.
17 Q. Cheng, J. Pang, D. Sun, J. Wang, S. Zhang, F. Liu, Y. Chen, R. Yang, N. Liang, X. Lu, Y. Ji, J. Wang, C. Zhang, Y. Sang, H. Liu and W. Zhou, *InfoMat*, 2020, **2**, 656–697.
18 A. Tomar, S. Issar, N. Choudhary, S. Kodan and R. Chandra, *Energy Fuels*, 2024, **38**, 13425–13435.
19 N. Choudhary, A. Tomar, S. Singh, R. Chandra and P. K. Maji, *Nanoscale*, 2025, **17**, 1289–1307.
20 J. Yang, C. Yu, X. Fan and J. Qiu, *Adv. Energy Mater.*, 2014, **4**, 1400761.
21 M. Jalili, H. Ghanbari, R. Malekfar and R. Goodarzi, *Phys. Status Solidi A*, 2023, **220**, 2300144.
22 A. Tomar, N. Choudhary, G. Malik and R. Chandra, *ACS Appl. Nano Mater.*, 2024, **7**, 26111–26125.
23 A. Aggarwal, M. Meier, E. Strangas and J. Agapiou, *Energies*, 2021, **14**, 6583.
24 A. Tomar, S. Issar, N. Choudhary, S. Kodan and R. Chandra, *Energy Fuels*, 2024, **38**, 13425–13435.
25 A. Tomar, N. Choudhary, G. Malik and R. Chandra, *ACS Appl. Nano Mater.*, 2024, **7**, 26111–26125.
26 L. Xia, L. Yu, D. Hu and G. Z. Chen, *Mater. Chem. Front.*, 2017, **1**, 584–618.
27 B. Pal, S. Yang, S. Ramesh, V. Thangadurai and R. Jose, *Nanoscale Adv.*, 2019, **1**, 3807–3835.
28 L. Xia, L. Yu, D. Hu and G. Z. Chen, *Mater. Chem. Front.*, 2017, **1**, 584–618.
29 T. S. Bhat, P. S. Patil and R. B. Rakhi, *J. Energy Storage*, 2022, **50**, 104222.
30 J. Zheng, J. A. Lochala, A. Kwok, Z. D. Deng and J. Xiao, *Adv. Sci.*, 2017, **4**, 1700032.
31 Y. Wang and W.-H. Zhong, *ChemElectroChem*, 2015, **2**, 22–36.
32 R. Tiwari, D. Kumar, D. K. Verma, K. Parwati, P. Ranjan, R. Rai, S. Krishnamoorthi and R. Khan, *J. Energy Storage*, 2024, **81**, 110361.
33 T. S. Bhat, P. S. Patil and R. B. Rakhi, *J. Energy Storage*, 2022, **50**, 104222.
34 M. S. Sokolikova, P. C. Sherrell, P. Palczynski, V. L. Bemmer and C. Mattevi, *Nat. Commun.*, 2019, **10**, 712.
35 A. Arora, P. Chander, A. Tomar, S. Kodan, R. Chandra and V. K. Malik, *ACS Appl. Electron. Mater.*, 2024, **6**, 3186–3196.
36 Y.-R. Peng, S.-Y. Tang, T.-Y. Yang, P. A. Sino, Y.-C. Chen, M. Chaudhary, C.-T. Chen, R.-H. Cyu, C.-C. Chung, B.-N. Gu, M.-J. Liu, C.-H. Hsu, H.-Y. Huang, L. Lee, S.-C. Wu, Y.-Y. Jen, Y.-S. Cheng, C.-C. Hu, W.-C. Miao, H.-C. Kuo and Y.-L. Chueh, *Adv. Energy Mater.*, 2023, **13**, 2301979.
37 M. S. Sokolikova, P. C. Sherrell, P. Palczynski, V. L. Bemmer and C. Mattevi, *Nat. Commun.*, 2019, **10**, 712.
38 X. Wang, Y. Chen, B. Zheng, F. Qi, J. He, Q. Li, P. Li and W. Zhang, *J. Alloys Compd.*, 2017, **691**, 698–704.
39 S. Singh, P. Gurawal, G. Malik, D. Kaur and R. Chandra, *Bull. Mater. Sci.*, 2024, **47**, 137.
40 J. H. Nam, M. J. Jang, H. Y. Jang, W. Park, X. Wang, S. M. Choi and B. Cho, *J. Energy Chem.*, 2020, **47**, 107–111.
41 D. Chakravarty and D. J. Late, *RSC Adv.*, 2015, **5**, 21700–21709.
42 S. Singh, P. Gurawal, G. Malik, R. Adalati, D. Kaur and R. Chandra, *Micro Nanostruct.*, 2024, **188**, 207794.
43 D. Singh, A. Singh, S. K. Ojha and A. K. Ojha, *Synth. Met.*, 2023, **293**, 117263.

 This journal is © The Royal Society of Chemistry 2025

Published on 24 2568. Downloaded on 7/6/2569 10:33:39.

44 H. Wang, D. Kong, P. Johanes, J. J. Cha, G. Zheng, K. Yan, N. Liu and Y. Cui, *Nano Lett.*, 2013, **13**, 3426–3433.
45 P. Martínez-Merino, E. Sani, L. Mercatelli, R. Alcántara and J. Navas, *ACS Sustainable Chem. Eng.*, 2020, **8**, 1627–1636.
46 Y. Fang, Y. Sun, B. Guo, H. Shen and R. Yang, *Ceram. Int.*, 2023, **49**, 28142–28150.
47 B. L. Chauhan, S. A. Bhakhar, P. M. Pataniya, S. U. Gupta, G. K. Solanki, V. M. Pathak and V. Patel, *J. Mater. Sci.: Mater. Electron.*, 2022, **33**, 10314–10322.
48 M. Xu, D. Li, Y. Yan, T. Guo, H. Pang and H. Xue, *RSC Adv.*, 2017, **7**, 43780–43788.
49 P. De, J. Halder, C. C. Gowda, S. Kansal, S. Priya, S. Anshu, A. Chowdhury, D. Mandal, S. Biswas, B. K. Dubey and A. Chandra, *Electrochem. Sci. Adv.*, 2023, **3**, e2100159.
50 N. Choudhary, A. Tomar, S. Singh, R. Chandra and P. K. Maji, *Nanoscale*, 2025, **17**, 1289–1307.
51 Z. Sun, B. Mei, H. Zhou, S. Qin and H. Zhang, *Ceram. Int.*, 2022, **48**, 25521–25527.
52 S. V. Kamat, V. Puri and R. K. Puri, *Int. Scholarly Res. Not.*, 2012, **2012**, 570363.
53 P. V. Mane, R. M. Rego, P. L. Yap, D. Losic and M. D. Kurkuri, *Prog. Mater. Sci.*, 2024, **146**, 101314.
54 S. Fu, Q. Fang, A. Li, Z. Li, J. Han, X. Dang and W. Han, *Energy Sci. Eng.*, 2021, **9**, 80–100.
55 E. Barsotti, S. P. Tan, S. Saraji, M. Piri and J.-H. Chen, *Fuel*, 2016, **184**, 344–361.
56 G. McHale, *Langmuir*, 2007, **23**, 8200–8205.
57 P. Kumar and D. J. E. Harvie, *Langmuir*, 2024, **40**, 16190–16207.
58 G. Wee, O. Larsson, M. Srinivasan, M. Berggren, X. Crispin and S. Mhaisalkar, *Adv. Funct. Mater.*, 2010, **20**, 4344–4350.
59 T. S. Bhat, P. S. Patil and R. B. Rakhi, *J. Energy Storage*, 2022, **50**, 104222.
60 H. Wu, X. Wang, L. Jiang, C. Wu, Q. Zhao, X. Liu, B. Hu and L. Yi, *J. Power Sources*, 2013, **226**, 202–209.
61 D. Lyu, K. Märker, Y. Zhou, E. W. Zhao, A. B. Gunnarsdóttir, S. P. Niblett, A. C. Forse and C. P. Grey, *J. Am. Chem. Soc.*, 2024, **146**, 9897–9910.
62 D. Werner, T. Alexander, D. Winkler, D. H. Apaydin, T. Loerting and E. Portenkirchner, *Isr. J. Chem.*, 2022, **62**, e202100082.
63 A. Bansal, P. Kumar, S. Issar, V. Chawla and R. Chandra, *Thin Solid Films*, 2024, **805**, 140506.
64 J.-S. M. Lee, M. E. Briggs, C.-C. Hu and A. I. Cooper, *Nano Energy*, 2018, **46**, 277–289.
65 H. Vijeth, S. P. Ashokkumar, L. Yesappa, M. Niranjana, M. Vandana and H. Devendrappa, *RSC Adv.*, 2018, **8**, 31414–31426.
66 R. Devi, V. Kumar, S. Kumar, M. Bulla and A. K. Mishra, *J. Energy Storage*, 2024, **79**, 110167.
67 A. Roy, A. Ray, S. Saha, M. Ghosh, T. Das, M. Nandi, G. Lal and S. Das, *Int. J. Energy Res.*, 2021, **45**, 16908–16921.
68 S. Wang, J. Zhu, Y. Shao, W. Li, Y. Wu, L. Zhang and X. Hao, *Chem. – Eur. J.*, 2017, **23**, 3438–3446.
69 P. Pazhamalai, K. Krishnamoorthy, V. K. Mariappan, S. Sahoo, S. Manoharan and S.-J. Kim, *Adv. Mater. Interfaces*, 2018, **5**, 1800055.
70 N. Choudhary, M. Patel, Y.-H. Ho, N. B. Dahotre, W. Lee, J. Y. Hwang and W. Choi, *J. Mater. Chem. A*, 2015, **3**, 24049–24054.
71 Q. Liu, J. Ning, H. Guo, M. Xia, B. Wang, X. Feng, D. Wang, J. Zhang and Y. Hao, *Nanomaterials*, 2021, **11**, 1477.
72 A. Khalil, Q. Liu, Q. He, T. Xiang, D. Liu, C. Wang, Q. Fang and L. Song, *RSC Adv.*, 2016, **6**, 48788–48791.
73 A. Ghorai, A. Midya and S. K. Ray, *New J. Chem.*, 2018, **42**, 3609–3613.
74 J. Li, Q. Shi, Y. Shao, C. Hou, Y. Li, Q. Zhang and H. Wang, *Energy Storage Mater.*, 2019, **16**, 212–219.
75 C. Hao, F. Wen, J. Xiang, L. Wang, H. Hou, Z. Su, W. Hu and Z. Liu, *Adv. Funct. Mater.*, 2014, **24**, 6700–6707.
76 X. Jian, H. Li, H. Li, Y. Li and Y. Shang, *Carbon*, 2021, **172**, 132–137.
77 N. Choudhary, C. Li, H.-S. Chung, J. Moore, J. Thomas and Y. Jung, *ACS Nano*, 2016, **10**, 10726–10735.